RNA Pol I activity is required for meiotic chromatin organization and the H3K4me3 gradient essential for oogenesis, independent of ribosome synthesis

Raquel Mejia-Trujillo*[1], Qiuxia Zhao*[1], Francesca Abraham[1], Ayesha Rahman[1], Elif Sarinay Cenik[1,†]

*Co-first authors

Affiliations

[1] Department of Molecular Biosciences, The University of Texas at Austin, Austin, TX 78712, USA

[†] Corresponding author: esarinay@utexas.edu

Lead contact

Requests for further information and resources should be directed to and will be fulfilled by the lead contact, Elif Sarinay Cenik (esarinay@utexas.edu).

GRAPHICAL ABSTRACT

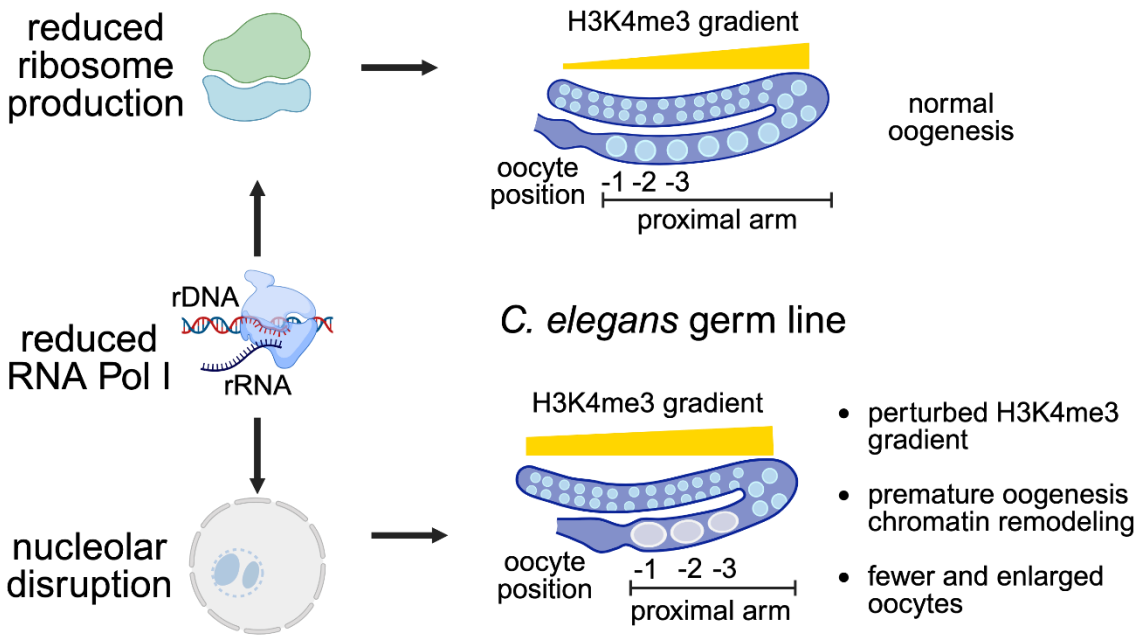

ABSTRACT

Oogenesis requires extensive and dynamic chromatin remodeling that primes gene promoters for later transcriptional activation during embryonic development. Here, we uncover a pivotal, non-canonical role for RNA Polymerase I (Pol I) in driving these chromatin state transitions during *Caenorhabditis elegans* oogenesis. Using the auxin-inducible degron system to selectively deplete either Pol I catalytic subunits or ribosome assembly factors, we disentangle the consequences of impaired nucleolar integrity from reductions in ribosome biogenesis. Strikingly, although disrupting ribosome assembly caused minimal effects on oocyte production, loss of Pol I activity led to widespread changes in chromatin accessibility, a dampening of the distal-proximal H3K4me3 gradient required for oogenesis, reduced synapsis, and elevated ATM/ATR phosphorylation, resulting in fewer but significantly larger oocytes. Despite their promoters becoming more accessible, oogenesis genes did not show large changes in steady-state mRNA, consistent with transcriptional repression prior to fertilization. Instead, Pol I depletion prematurely remodeled oogenic chromatin, through a misdirection of H3K4me3 deposition towards promoters normally primed for zygotic genome activation. These findings reveal an epigenetic gating function for nucleolar integrity in oocyte maturation: Pol I preserves three-dimensional chromatin organization and maintains proper spatiotemporal regulation of histone modifications, independent of ribosome production. Given the evolutionary conservation of nucleolar dynamics and histone modifications during gametogenesis, our work suggests that nucleolar stress, whether from environmental factors, aging, or genetic disorders, could broadly compromise fertility by disrupting oogenic chromatin priming.

INTRODUCTION

Chromosome condensation and chromatin modifications during meiosis are essential to ensure accurate genetic transmission in sexually reproducing species. In the hermaphroditic germ line of *Caenorhabditis elegans*, female gamete production proceeds through four distinct zones: mitotic proliferation, transition, meiosis I, and oocyte maturation. Upon completion of oocyte maturation, the most proximal oocyte is fertilized by the adjacent spermatheca, initiating zygotic development.

Oogenesis involves a complex progression of germ cell maturation, yet net transcriptional activity is strikingly low in late-stage oocytes. Instead, many oogenesis genes remain largely quiescent before fertilization, with regulation relying primarily on extensive chromatin remodeling. This epigenetic priming prepares the promoters of key developmental genes to be robustly activated after fertilization or during early embryogenesis [1–3].

In *C. elegans*, as in other species, germ cells undergo profound chromatin reorganization during meiotic progression to form specialized meiotic chromatin structures, establish parental imprinting marks, and position active marks near the promoters of genes that will be engaged during zygotic genome activation (ZGA) [4]. Specifically, H3K4me3 marks shift from gene bodies to promoters as undifferentiated mitotic germ cells progress through meiosis I [4]. This promoter-specific priming of ZGA genes with H3K4me3 is evolutionarily conserved across species, including *Xenopus* [5], zebrafish [6,7], mice [8,9], and humans [10] and is critical for normal germ line development. For instance, *C. elegans* germ lines lacking H3K4 methyltransferase activity exhibit reduced oocyte production, aberrant nuclear morphology, and aneuploid gametes [11,12], while deficient H3K4 demethylase activity leads to abnormal chromatin condensation, diminished oocyte production, and failed entry into meiosis [13].

In parallel with the spatiotemporal regulation of H3K4 methylation, maturing germ cells also temporally regulate nucleolar activity during oogenesis. The nucleolus, responsible for rRNA synthesis and ribosome assembly [14], remains intact throughout meiosis but temporarily disassembles at the onset of oocyte maturation before reappearing during ZGA [15]. Similar nucleolar dynamics have been documented across hermaphrodite and dioecious eukaryotes, including *C. elegans*, yeast, pig, and mouse [15–20]. The presence of the nucleolus throughout oogenesis is unsurprising [21], given that maternal ribosome production is sufficient to drive embryogenesis in *Caenorhabditis elegans* [22]; however, the nucleolus may have additional roles beyond ribosome production during oogenesis. For example, in *Arabidopsis*, rDNA loci are embedded within the nucleolus to prevent alterations of rDNA copy numbers and genomic instability during meiotic homologous recombination [23]. In mouse oocytes, maternal nucleolar components are essential for

63 maintaining satellite repeat sequences immediately after fertilization [24]. Lastly, the nucleolar
64 microenvironment in *C. elegans* can sequester transcriptional silencing factors, such as PIE-1, away from
65 the genome to promote transcription during late oogenesis [25].

66 Despite these hints of broader functions for the nucleolus, dissecting its direct contributions to oogenesis
67 has been challenging because rRNA synthesis, ribosome assembly, and the maintenance of a spatially
68 distinct nuclear subcompartment are all interconnected. For example, RNA Polymerase I (Pol I)
69 transcription of rDNA loci is accompanied by co-transcriptional processing of pre-rRNA, followed by co-
70 assembly with ribosomal proteins into ribosome subunits [26]. The nucleolar microenvironment is similarly
71 co-dependent on these other functions, as its liquid-liquid phase-separated properties make its spherical
72 morphology reliant on active rDNA transcription and subsequent processing and assembly [27,28]. Thus,
73 similar to how separation-of-function mutations in proteins are used to differentiate between distinct protein
74 functions [29–31], there is a demand for genetic tools that can isolate interconnected functions of the same
75 subcellular structure. Here, we utilized separation-of-function *C. elegans* strains to identify potential
76 nucleolar functions that are independent from ribosome production during oogenesis.

77 Using the auxin-inducible degron (AID) system, we targeted either two catalytic subunits specific to RNA
78 Pol I (orthologous to human *POL1RA* and *POL1RB*) or two ribosome assembly factors essential for 60S
79 and 40S assembly (orthologous to human *GRWD1* and *TSR2,* respectively). This approach isolates the
80 impact of nucleolar disruption on female germ cell maturation from perturbed downstream ribosome
81 assembly. Our results uncover a non-ribosomal function of RNA Pol I in regulating oocyte production,
82 meiotic chromosome morphology and chromatin landscape, and the maintenance of an essential H3K4
83 methylation gradient. Germ cells fail to regulate chromatin remodeling during the transition from mitotic
84 proliferation to meiotic prophase I following reduced RNA Pol I activity, but not after a decrease in
85 ribosome assembly. ATAC-seq analyses further reveal that chromatin accessibility increases near oogenesis
86 promoters, oogenesis-promoting EFL-1-binding sites, and promoters subject to canonical H3K4me3
87 remodeling during oogenesis. Nucleolar disruption induced upon RNA Pol I depletion also dampened the
88 distal-proximal H3K4me3 gradient through premature H3K4me3 deposition and resulted in increased
89 ATM/ATR phosphorylation in the pachytene region of the germ line. Collectively, our data suggests that
90 nucleolar integrity, maintained by RNA Pol I activity, is involved in the coordination of chromatin
91 remodeling during oogenesis, ensuring the production of healthy, properly sized oocytes.

92 **RESULTS**

93 **Persistence and dynamics of nucleolar structure during *Caenorhabditis elegans* germ line**
94 **development and oogenesis**

95 We first examined nucleolar morphology in a wild-type background to establish a baseline representation
96 of its structure during germ line development, from the mitotic through meiotic zones, and into oocyte
97 maturation. To accomplish this, we fluorescently tagged two genes: *nucl-1*, the *Caenorhabditis elegans*
98 ortholog of human *NCL*, which facilitates rRNA transcription and processing [32–34], and *dao-5*, the ortholog
99 of human *NOLC1*, required for nucleologenesis and rDNA transcription [15,35.] We also used a fluorescent
100 SYP-3 reporter, a key component of the synaptonemal complex [36,37], to distinguish between different germ
101 line zones. Cells distal to synaptonemal complex formation were classified as mitotic, cells displaying a
102 synaptonemal complex were assigned to the transition or pachytene zone, and cells with visible plasma
103 membrane under transmitted photomultiplier tubes (T-PMT) were defined as being in the oocyte maturation
104 zone.

105 In a mature germ line, NUCL-1 retains a spherical nucleolar localization pattern in the mitotic, meiotic, and
106 most of the oocyte maturation zone (**Figure S1A**). As the oocytes matured, the nucleolus formed
107 intermediate droplet-like structures in the "-2" oocyte (the second-most proximal oocyte), followed by
108 complete dissolution in the "-1" oocyte (the most proximal one) (**Figure S1B**). These results suggest that
109 nucleolar integrity is largely maintained from the distal mitotic region through meiosis but is disrupted just
110 before fertilization. This observation agrees with previous reports in *C. elegans* germ lines [15,38,39] and is also
111 conserved in mammalian oocytes [16,18–20].

Supplementary Figure 1

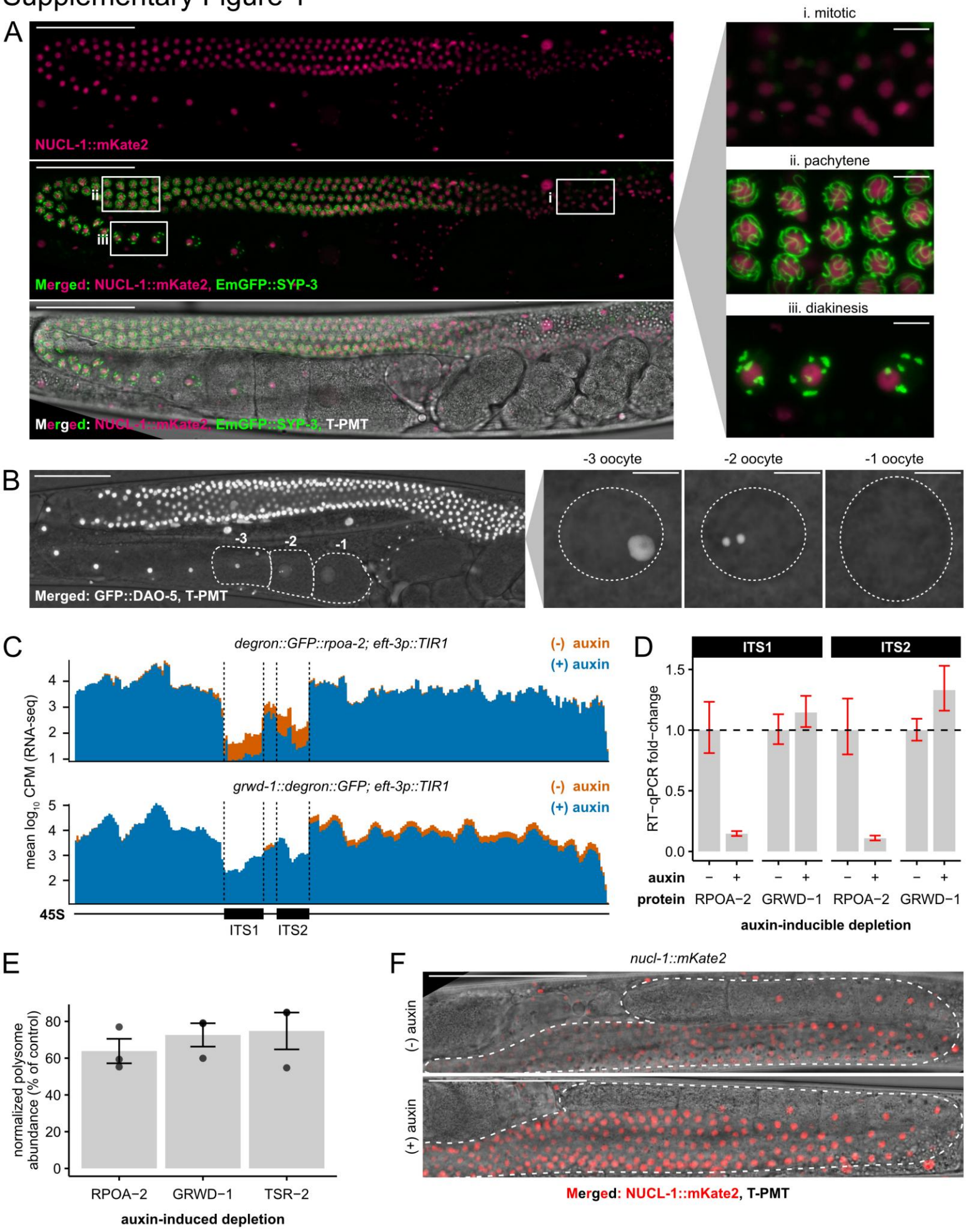

113 **Figure S1, Related to Figure 1. Nucleolar dynamics throughout the germ line (A, B, F); effects of**
114 **Pol I and ribosome assembly chaperone depletion on the transcription of internally transcribed**
115 **spacers (ITS) and downstream polysome abundance (C-E).**

116 (**A**) Average confocal projection of an adult germ line (left) with an endogenous NUCL-1::mKate2
117 nucleolar marker and an EmGFP::SYP-3 meiosis marker. Nucleoli are present throughout the mitotic,
118 pachytene, and diakinesis zones (right), as indicated by the localization of EmGFP::SYP-3. Scale bar = 50
119 µm (full germ line) and 5 µm (zoom). (**B**) Average confocal projection of an adult germ line (left) with an
120 endogenous GFP::DAO-5 nucleolar marker. Zoomed in nuclei (right) reveal that the nucleolus forms
121 droplets in the "-2" oocyte and is absent in the most proximal and mature "-1" oocyte. Scale bar = 50 µm
122 (germ line) and 5 µm (nuclei). (**C**) Average $\log_{10}$ counts per million (CPM) reads from gonadal RNA-seq
123 (total RNA) mapped to a simplified single-copy 45S rDNA locus. Averages are composed of three
124 biological replicates per condition, each consisting of 20 gonads. RPOA-2-depleted germ lines show
125 reduced coverage across internally transcribed spacer (ITS) regions compared to GRWD-1-depleted germ
126 lines. (**D**) RT-qPCR analysis of whole-animal ITS1 and ITS2 expression following auxin-inducible
127 depletion of RPOA-2/GRWD-1. Relative transcript levels of ITS1 and ITS2 were normalized to mature
128 26S rRNA. Data represent three biological replicates for RPOA-2 depletion and two biological replicates
129 for GRWD-1 depletion, with three technical replicates per biological replicate. Bars and error bars represent
130 mean ± SD. (**E**) Polysome abundance after auxin-induced depletion of RPOA-2, GRWD-1, and TSR-2,
131 normalized to the abundance of free RNA. Points represent biological replicates (3 per condition); bars and
132 error bars represent the mean and SEM, respectively. (**F**) NUCL-1::mKate2 is morphologically unaffected
133 by 1 mM IAA in a wild-type background. Scale bar = 50 µm.

134 **Disruption of RNA Pol I activity compromises nucleolar structure throughout the germ line**

135 Having established that a spherical nucleolus persists through most of germ line development in mature
136 hermaphrodites, we next asked how reducing rDNA transcription would affect its structure. Nucleolar
137 integrity depends on robust RNA polymerase I (Pol I) activity, as the formation of nucleolar
138 subcompartments and phase separation properties are largely driven by elevated concentrations of rRNA,
139 along with its bound nucleolar factors [27,28,40]. Although prior work in the *C. elegans* germ line utilized
140 Actinomycin D to inhibit rDNA transcription, no visible disturbance of nucleolar structure was detected,
141 likely because transcription was not suppressed below a critical threshold associated with nucleolar
142 segregation [41,42]. Thus, to clearly disrupt nucleolar structure, we used the auxin-inducible degron (AID)
143 system to substantially deplete two endogenously tagged subunits of RNA Pol I: RPOA-1, the largest

144 subunit of RNA Pol I (orthologous to human *POLR1A*), and RPOA-2, a catalytic subunit specific to RNA
145 Pol I (orthologous to human *POLR1B*) [38,43].

146 Animals expressing degron::GFP::RPOA-2 and RPOA-1::degron::GFP were treated with 1 mM IAA
147 (auxin) at the L4 stage for 18 hours, after which gonads from young adults were dissected and examined
148 by fluorescent microscopy. A significant decrease in mean GFP intensity confirmed a substantial depletion
149 of both RPOA-1 and RPOA-2 in germ cells (**Figure 1A-B** and **1E**). To confirm that this depletion impaired
150 rDNA transcription, we performed RNA-seq on gonadal samples using total RNA and quantified the
151 abundance of reads mapping to two loci uniquely found in nascent pre-rRNA. We observed a significant
152 decrease in reads mapping to the internally transcribed spacers (ITS1 and ITS2), indicating a considerable
153 decrease in RNA Pol I activity upon depletion of RPOA-2 (**Figure 1F** and **S1C**, one-tailed Welch two-
154 sample *t*-test, 4.6-fold average decrease for ITS1: $p = 0.021$, 1.6-fold average reduction for ITS2: $p =$
155 0.0092). RT-qPCR also supports that the depletion of RPOA-2 significantly reduces pre-rRNA synthesis
156 **(Figure S1D**, left-tailed paired Student's *t*-test, ITS1: $p = 0.0048$, ITS2: $p = 0.0015$**).**

157 We next investigated whether these transcriptional reductions could sufficiently disrupt spherical nucleolar
158 structure, identifiable by the formation of nucleolar caps [42]. In RPOA-2-depleted gonads, the nucleolar
159 marker NUCL-1::mKate2, showed droplet and cap-like structures throughout the germ line, in contrast to
160 the more uniform spherical nucleoli in control animals (**Figure 1G**). This phenotype suggests that the
161 threshold of rDNA transcription required for nucleolar integrity was not met upon RPOA-2 depletion,
162 leading to a clear disruption of nucleolar morphology. We validated that auxin treatment alone did not
163 induce any unintended morphological changes to gonadal NUCL-1::mKate2 in the absence of the AID
164 system (**Figure S1F**).

165 Although RPOA-2 depletion disrupts nucleolar structure by reducing rRNA synthesis, it also suspends
166 ribosome production, which might impact the translational capacity of developing germ cells [43]. Despite
167 the generally low transcriptional activity of germ cells, proper ribosome production is essential for
168 translational regulation of gene expression and maternal ribosome loading to ensure embryonic viability
169 [22,44–46]. Importantly, our prior work indicates that both the depletion of RPOA-2 or ribosome assembly
170 factors result in a comparable decrease in overall ribosome production, as evidenced by developmental
171 arrest on auxin [43]. Thus, to separate the effects of nucleolar disruption from potential consequences of
172 ribosome biogenesis disruption, we conducted identical experiments using endogenous fluorescently-
173 labeled AID strains for GRWD-1, a chaperone that guides RPL-3 assembly into the 60S ribosomal subunit
174 [43,47], and TSR-2, a chaperone that incorporates RPS-26 into the 40S subunit [48].

175 Following auxin treatment of L4 animals, we observed a significant decrease in GRWD-1::degron::GFP
176 and TSR-2::degron::GFP intensity in germ lines, confirming the depletion of both ribosome assembly
177 factors (**Figure 1C-E**). However, RNA-seq analyses revealed no significant reduction in ITS1 and ITS2
178 pre-rRNA reads, suggesting that the depletion of ribosome assembly factors does not impair rRNA
179 synthesis mediated by RNA Pol I activity (**Figure 1F** and **S1C**, one-tailed Welch's two-sample *t*-tests;
180 GRWD-1: 1.4-fold average increase in ITS1: $p = 0.99$, 1.4-fold average decrease in ITS2: $p = 0.16$; TSR-
181 2: 1.1-fold average increase in ITS1: $p = 0.37$, no average fold-change in ITS2: $p = 0.54$). Instead, consistent
182 with prior observations involving RPL-3 reduction, the ITS1 intermediate accumulated under GRWD-1
183 depletion (**Figure S1B**) [21]. Such accumulation is similar to that reported in other systems, where defects in
184 60S assembly result in the accumulation of 40S-associated pre-rRNA intermediates containing ITS1
185 sequences [49]. RT-qPCR also validated that pre-rRNA synthesis does not decrease upon GRWD-1 depletion
186 (**Figure S1D**, left-tailed paired Student's *t*-test, ITS1: 0.67, ITS2: $p = 0.99$). Furthermore, the nucleolar
187 morphology in GRWD-1-depleted germ lines appeared vacuolated yet retained a persistent spherical form,
188 similar to the morphology observed when RPL-3 is reduced (**Figure 1H**) [21]. Polysome profiling further
189 indicates that global translation levels are similarly reduced upon depletion of RPOA-2, GRWD-1, or TSR-
190 2 (**Figure S1E**).

191 Together, these findings support the conclusion that although RPOA-2 and GRWD-1 depletion both reduce
192 ribosome biogenesis, only impaired rRNA transcription, mediated by a disruption of RNA Pol I activity,
193 disrupts spherical nucleolar structure throughout the germ line. This result highlights a specific requirement
194 for RNA Pol I activity in maintaining nucleolar morphology during oogenesis, independent of downstream
195 ribosome assembly.

Figure 1

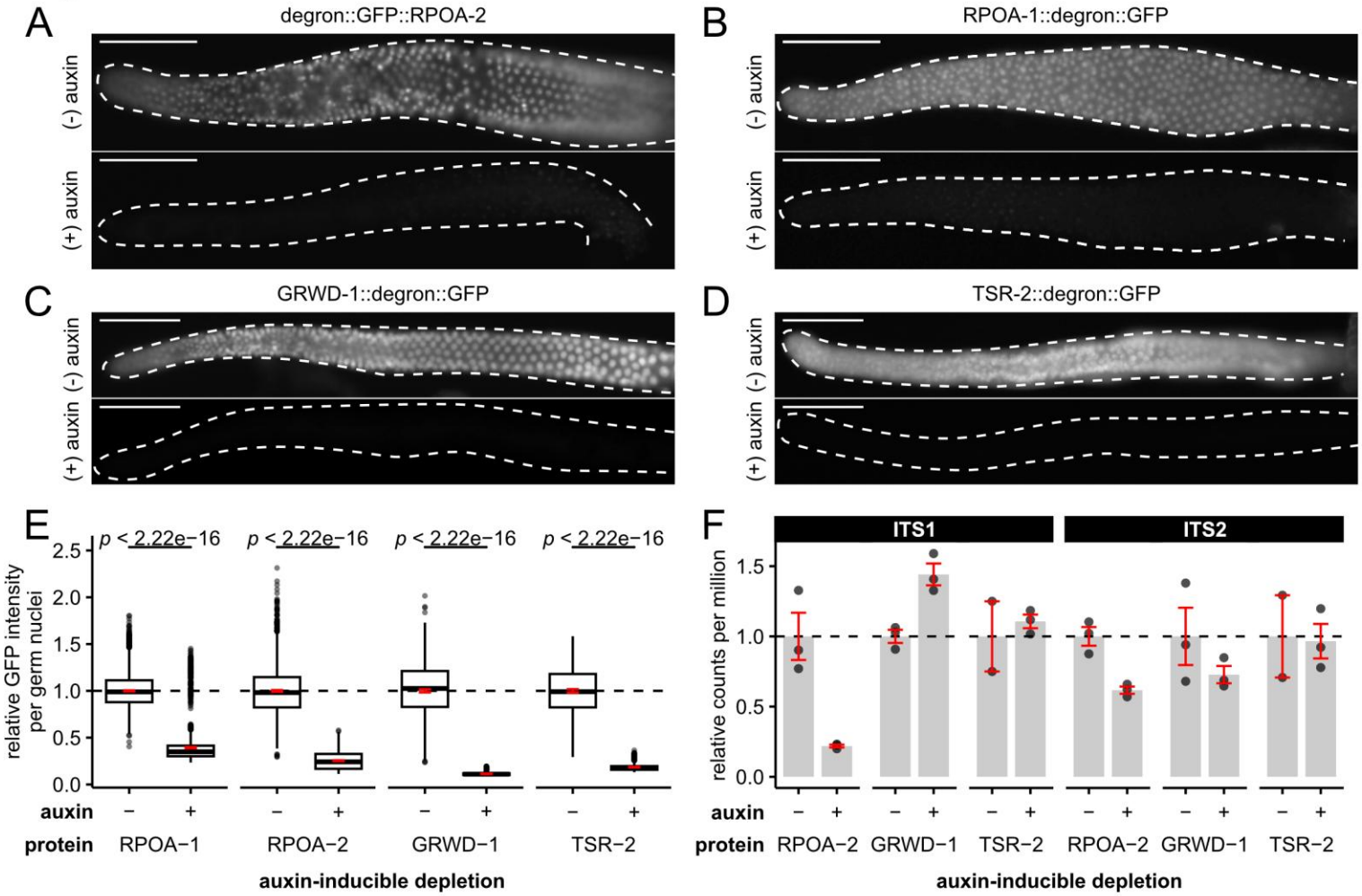
A
degron::GFP::RPOA-2
(-) auxin
(+) auxin
B
RPOA-1::degron::GFP
(-) auxin
(+) auxin
C
GRWD-1::degron::GFP
(-) auxin
(+) auxin
D
TSR-2::degron::GFP
(-) auxin
(+) auxin
E
p < 2.22e−16
p < 2.22e−16
p < 2.22e−16
p < 2.22e−16
relative GFP intensity per germ nuclei
2.5
2.0
1.5
1.0
0.5
0.0
auxin − + − + − + − +
protein RPOA−1 RPOA−2 GRWD−1 TSR−2
auxin-inducible depletion
F
ITS1
ITS2
relative counts per million
1.5
1.0
0.5
0.0
auxin − + − + − + − + − + − +
protein RPOA−2 GRWD−1 TSR−2 RPOA−2 GRWD−1 TSR−2
auxin-inducible depletion

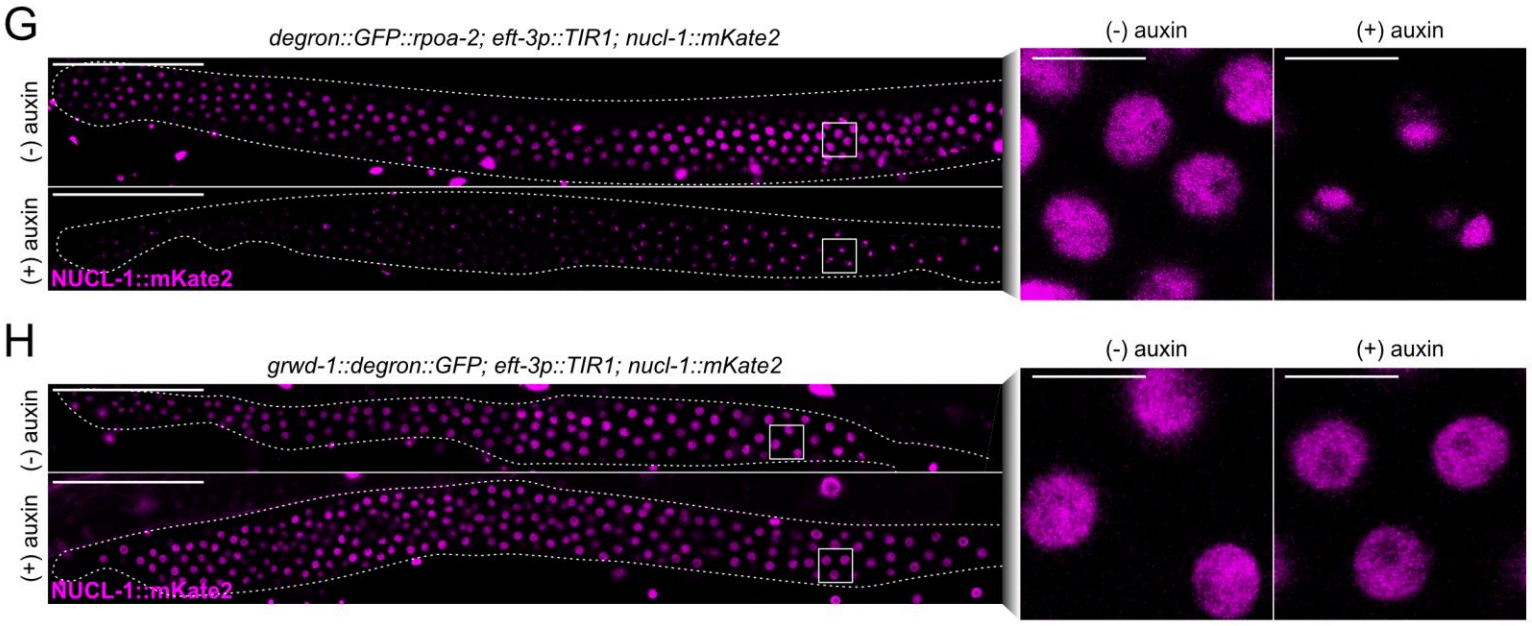
G
degron::GFP::rpoa-2; eft-3p::TIR1; nucl-1::mKate2
(-) auxin
(+) auxin
(-) auxin
(+) auxin
NUCL-1::mKate2
H
grwd-1::degron::GFP; eft-3p::TIR1; nucl-1::mKate2
(-) auxin
(+) auxin
(-) auxin
(+) auxin
NUCL-1::mKate2

197 **Figure 1. Auxin-inducible depletion of RNA Pol I subunits and ribosome assembly factors reveal**
198 **that nucleolar structure is dependent on pre-rRNA synthesis but not downstream ribosome**
199 **maturation. See also Figure S1.**

200 (**A-D**) Germline expression of fluorescently tagged RPOA-2 (**A**), RPOA-1 (**B**), GRWD-1 (**C**), and TSR-2
201 (**D**) proteins after control or auxin treatment. Dissected germ lines are outlined in white. Each strain's
202 control/auxin images were taken with identical exposure settings. Scale bar = 50 µm. (**E**) Distribution of
203 germ nuclei GFP intensity after auxin-inducible depletion of GFP-tagged RPOA-1/RPOA-2/GRWD-
204 1/TSR-2. Statistical comparisons performed using left-tailed Welch's two-sample *t*-tests. (**F**) Comparisons
205 of counts per million (CPM) reads across a simplified single copy of the ITS1 and ITS2 loci based on
206 gonadal RNA-seq (total RNA) after auxin-inducible depletion of RPOA-2/GRWD-1/TSR-2. Points
207 represent biological replicates (3 per condition, each consisting of 20 gonads); bars and error bars represent
208 the mean and SEM, respectively. (**G-H**) Germline nucleolar morphology (endogenous NUCL-1::mKate2)
209 after auxin-inducible depletion of RPOA-2 (**G**) or GRWD-1 (**H**). Germ lines are outlined in white; zoomed-
210 in nucleoli are shown in the right column. Scale bars = 50 µm (whole gonad) and 5 µm (zoomed nucleoli).

211 **RNA Pol I activity plays a ribosome-biogenesis-independent role in maintaining oocyte production**
212 **and morphology**

213 To investigate whether germ cells remain viable when RNA Pol I activity and ribosome assembly are
214 reduced, we stained animals with acridine orange to label cell corpses following auxin-inducible depletion
215 of RPOA-2, GRWD-1, or TSR-2. We did not observe any differences in cell corpse abundance in any of
216 our treatments (**Figure S2A-B**), suggesting that apoptosis was not induced during this time frame. Given
217 that germ cells remained viable, we next examined whether germ line maturation was affected upon
218 reductions in Pol I activity or ribosome biogenesis by measuring proximal arm length, the number of
219 proximal oocytes, and the dimensions of the three most proximal oocytes (**Figure 2A-B**). We also
220 normalized proximal arm length to overall body area (**Figure 2C)**, given that the global AID system can
221 reduce body size due to high basal degradation in the absence of auxin, particularly in the GRWD-1 and
222 TSR-2 AID strains [43] (**Figure 2A, S2C**).

223 Reductions in Pol I activity (mediated by RPOA-1 or RPOA-2 depletion), but not reductions in ribosome
224 assembly (mediated by GRWD-1 or TSR-2 depletion), uniquely reduced the length of the proximal arm
225 (**Figure 2A-B**), diminished the number of proximal oocytes (**Figure 2A** and **2D**), and caused the three most
226 proximal oocytes to occupy a significantly larger fraction of the proximal arm (**Figure 2A** and **2E**). These
227 results suggest that oocyte production and morphology are disrupted specifically by reducing RNA Pol I
228 activity, rather than by impairing ribosome assembly.

Supplementary Figure 2

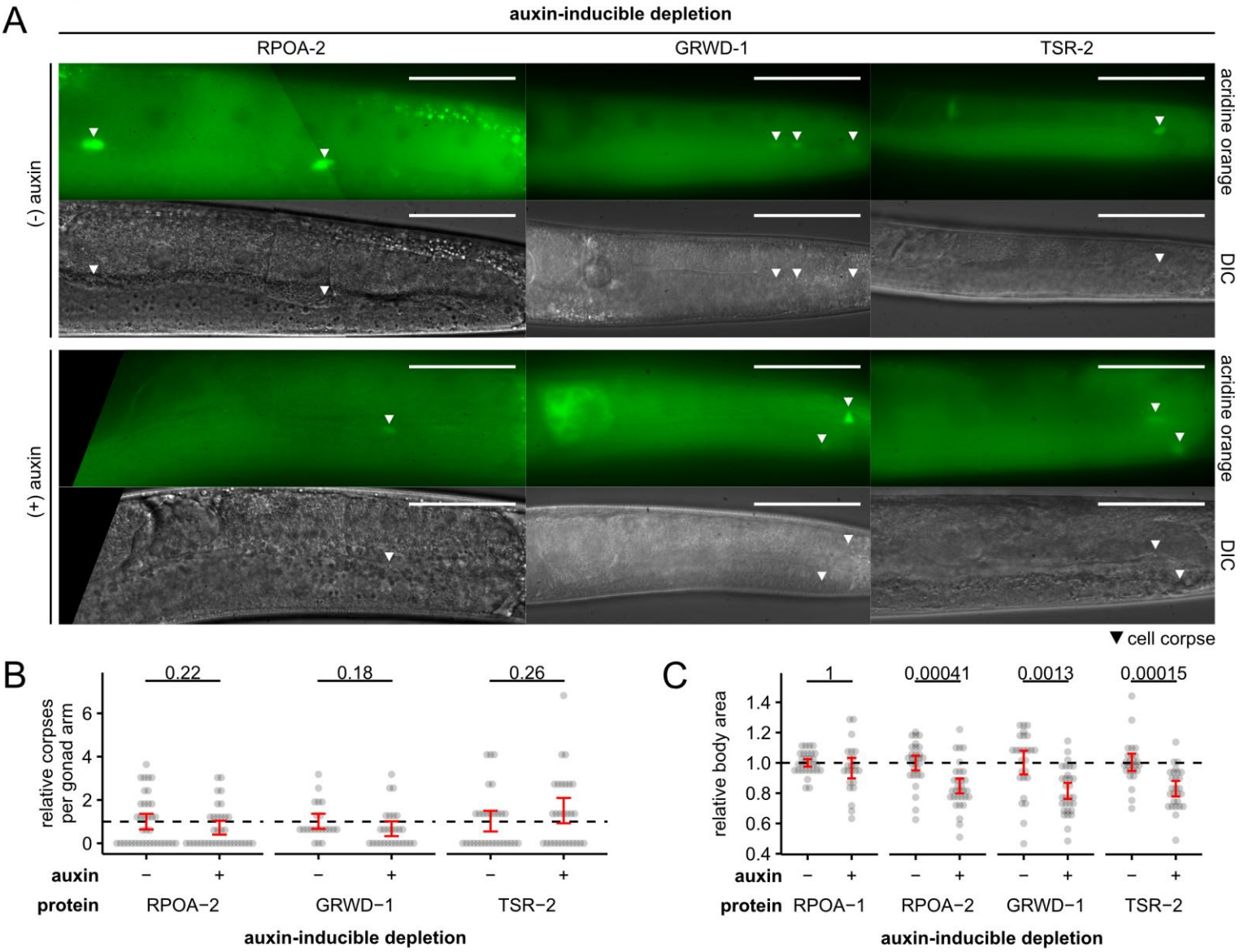

Figure S2, Related to Figure 2. Effects on germ cell death and animal body area under reduced RNA Pol I activity or ribosome assembly.

(**A**) Acridine-orange-stained germ lines after auxin-inducible depletion of RPOA-2/GRWD-1/TSR-2. Cell corpses are indicated by white triangles; gonad arms are outlined in white. Scale bar = 50 µm. (**B**) Distribution of cell corpses per gonad arm based on acridine orange staining, normalized to the mean of each strain's control group. Each point represents the number of corpses in a gonad arm across three biological replicates. Statistical comparisons performed using a two-tailed Welch's two-sample *t*-test. (**C**) Distribution of body areas after auxin-inducible depletion of RPOA-1/RPOA-2/GRWD-1/TSR-2. Each point represents measurements from an individual worm, normalized to the mean of each strain's control group. Crossbars represent SEM. Statistical comparisons performed using a left-tailed Welch's two-sample t-test with Bonferroni corrections.

Figure 2

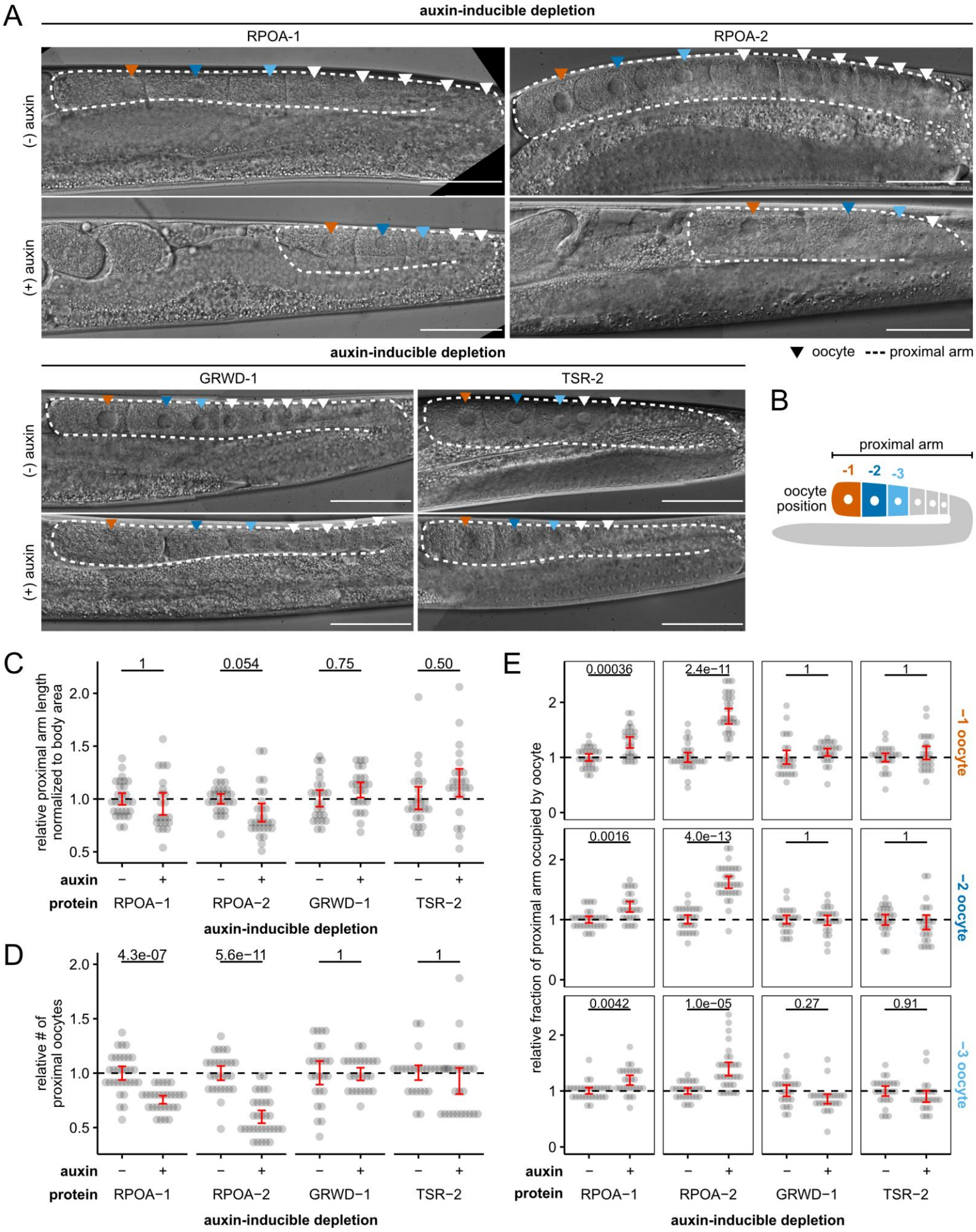
A
auxin-inducible depletion
RPOA-1
RPOA-2
(-) auxin
(+) auxin
auxin-inducible depletion
GRWD-1
TSR-2
(-) auxin
(+) auxin
oocyte
proximal arm
B
proximal arm
-1
-2
-3
oocyte position
C
relative proximal arm length normalized to body area
1
0.054
0.75
0.50
auxin
protein
RPOA−1
RPOA−2
GRWD−1
TSR−2
auxin-inducible depletion
D
relative # of proximal oocytes
4.3e-07
5.6e−11
1
1
auxin
protein
RPOA−1
RPOA−2
GRWD−1
TSR−2
auxin-inducible depletion
E
relative fraction of proximal arm occupied by oocyte
0.00036
2.4e−11
1
1
−1 oocyte
0.0016
4.0e−13
1
1
−2 oocyte
0.0042
1.0e−05
0.27
0.91
−3 oocyte
auxin
protein
RPOA−1
RPOA−2
GRWD−1
TSR−2
auxin-inducible depletion

242 **Figure 2. Oocyte morphology and organization are impaired by reduced RNA Pol I activity,**
243 **independent from RNA Pol I's role in ribosome production. See also Figure S2.**

244 (**A**) Representative DIC images of adult germ lines after auxin-inducible depletion of RPOA-1/RPOA-
245 2/GRWD-1/TSR-2. Dotted lines highlight the proximal arm; triangles point to proximal oocytes. Scale bar
246 = 50 µm. (**B**) Graphical representation of proximal arm length and oocyte positions quantified in (**C-E**).
247 (**C-E**) Proximal arm lengths (**C**), proximal oocyte counts (**D**), and oocyte sizes (**E**) after auxin-inducible
248 depletion of RPOA-1/RPOA-2/GRWD-1/TSR-2. Each point represents a measurement from an individual
249 animal, normalized to the mean of each strain's control group. Crossbars represent SEM. All comparisons
250 were performed using two-tailed Welch's two-sample *t*-tests followed by Bonferroni corrections.

251 **Impaired synapsis reveals a Pol I-dependent sensitivity to nucleolar stress during the mitotic-to-**
252 **meiotic transition**

253 The observation that reduced RNA Pol I activity, but not impaired ribosome assembly, leads to defects in
254 oocyte maturation prompted us to investigate how each condition affects meiotic progression. Using a
255 fluorescently tagged SYP-3, a component of the synaptonemal complex [36,37], we determined whether germ
256 cells adopted characteristic DNA morphology in the mitotic, transition, and meiotic zones. We assessed the
257 appearance of crescent shaped nuclei in the transition zone, where DNA and the nucleolus cluster to
258 opposite nuclear poles, and whether chromosomes in the meiotic zone were repositioned to the nuclear
259 periphery.

260 Following auxin-inducible depletion of RPOA-2, germ cells entering the mitotic-to-meiotic transition zone
261 showed reduced polarization and SYP-3 assembly, likely reflecting a lack of synaptonemal complex
262 formation; however, the downstream re-localization of synapsed chromosomes to the nuclear periphery in
263 proximal germ cells remained unaffected (**Figure 3A, S3)**.

264 These differences raised the possibility that nucleolar integrity is critical for proper chromosome
265 morphology during meiotic entry. Specifically, in transition zone nuclei, the nucleolus and chromosomes
266 segregate to opposite poles, likely to facilitate homolog pairing by bringing homologous chromosomes into
267 proximity [50–52]. To determine whether perturbing nucleolar structure or activity, rather than bulk ribosome
268 synthesis, affects this characteristic crescent shaped chromosome polarization, we depleted key ribosome
269 synthesis and nucleolar factors by RNA interference (RNAi). We first validated RNAi efficacy by injecting
270 double-stranded RNA targeting *rpoa-2, grwd-1, fib-1* (human *FBL* ortholog), and *nucl-1*, and monitored
271 protein depletion using fluorescent tagged reporters. All four proteins were effectively depleted to near-

272 background levels within 48 hours (**Figure S4A-D**). We then used these validated RNAi conditions on an
273 EmGFP::SYP-3 and NUCL-1::mKate2 reporter strain to examine synaptonemal complex assembly and
274 chromatin architecture throughout meiotic prophase (**Figure 3B**, **S4E**). Depletion of *rpoa-2* and *fib-1*
275 resulted in similar germline deficiencies, including less transition zone polarization **(Figure 3B, S4E)**, a
276 reduction of transition zone SYP-3 aggregation (indicative of impaired synapsis) **(Figure 3B, S4E),** and a
277 reduction of proximal oocytes **(Figure S4F, 2A).** In contrast, *nucl-1* knockdown resulted in no detectable
278 defects in either chromosome polarization or synapsis. Similarly, although knockdown of *grwd-1* decreased
279 overall SYP-3 intensity, SYP-3 aggregation and transition zone polarization remained largely comparable
280 to non-target RNAi injected gonads (**Figure 3B**, **S4E**). In addition, we did not observe any differences in
281 the redistribution of SYP-3 to the nuclear periphery in late pachytene/post transition zone nuclei in any of
282 the knockdowns (**Figure S4E**), likely suggesting that newly transitioning nuclei are receptive to nucleolar
283 stress.
284 Together, these results support that nuclei entering the mitotic-to-meiotic transition zone are sensitive to
285 nucleolar functions dependent on RNA Pol I activity (RPOA-2 and FIB-1) rather than downstream
286 ribosome processing steps (NUCL-1 and GRWD-1), supported by Pol-I dependent defects in transition
287 zone polarization and synaptonemal complex assembly.

Figure 3

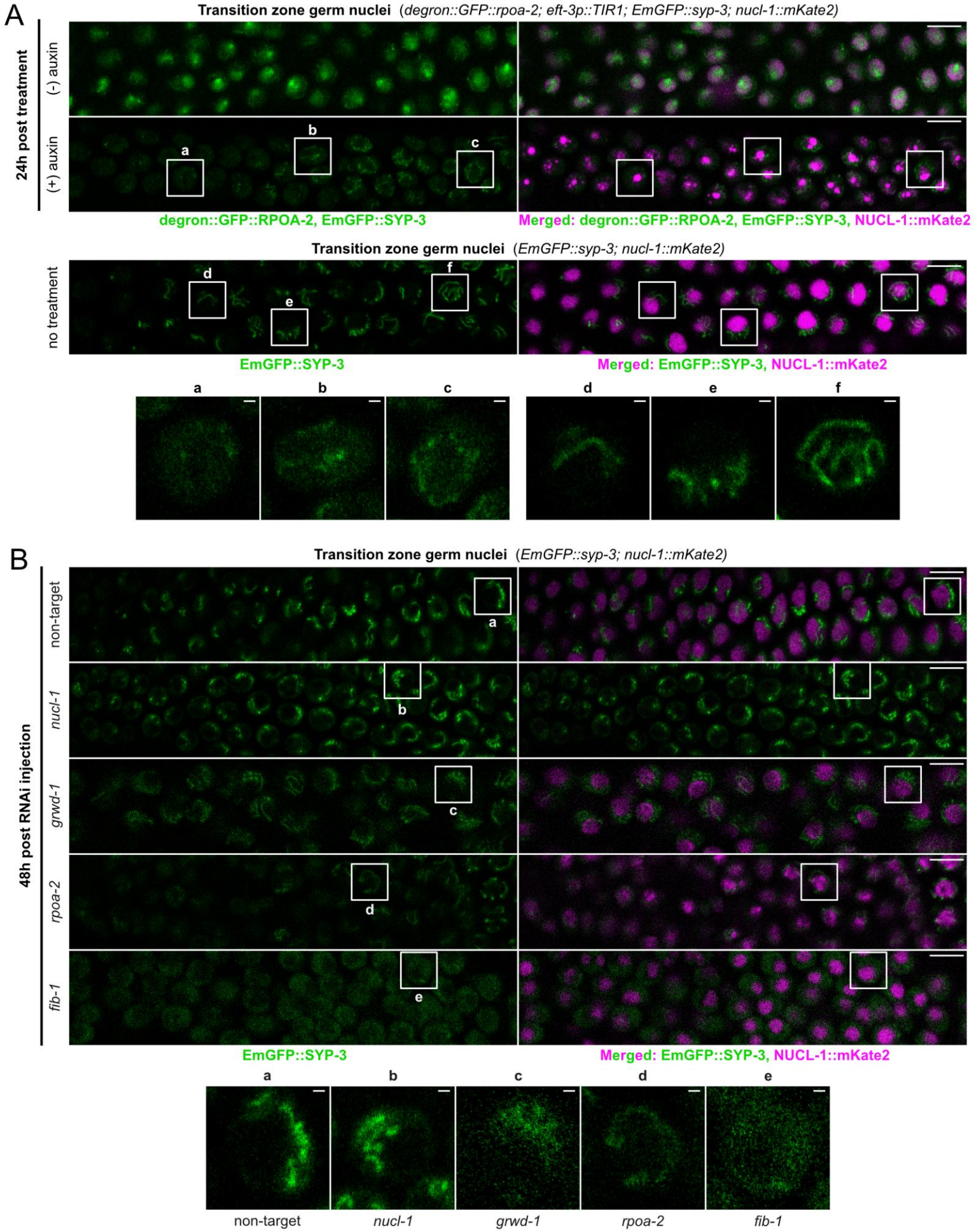
A
Transition zone germ nuclei (degron::GFP::rpoa-2; eft-3p::TIR1; EmGFP::syp-3; nucl-1::mKate2)
24h post treatment
(-) auxin
(+) auxin
a
b
c
degron::GFP::RPOA-2, EmGFP::SYP-3
Merged: degron::GFP::RPOA-2, EmGFP::SYP-3, NUCL-1::mKate2
Transition zone germ nuclei (EmGFP::syp-3; nucl-1::mKate2)
no treatment
d
e
f
EmGFP::SYP-3
Merged: EmGFP::SYP-3, NUCL-1::mKate2
a
b
c
d
e
f
B
Transition zone germ nuclei (EmGFP::syp-3; nucl-1::mKate2)
48h post RNAi injection
non-target
nucl-1
grwd-1
rpoa-2
fib-1
a
b
c
d
e
EmGFP::SYP-3
Merged: EmGFP::SYP-3, NUCL-1::mKate2
a
b
c
d
e
non-target
nucl-1
grwd-1
rpoa-2
fib-1

289 **Figure 3. Synaptonemal complex formation during the mitotic-to-meiotic germ cell transition is**
290 **dependent on Pol I activity, but not other ribosome processing steps. See also Figure S3 and S4.**

291 **(A)** Confocal images of transition zone nuclei expressing degron::GFP::RPOA-2, EmGFP::SYP-3, and
292 NUCL-1::mKate2 following control or auxin-inducible depletion of RPOA-2 (top two rows). Additionally,
293 we show non-treated nuclei from a wild-type genetic background (middle row) and zoomed-in nuclei from
294 RPOA-2-depleted and wild-type conditions (bottom row, labeled a-e). Scale bar = 5 µm (transition zone)
295 and 0.5 µm (zoomed-in nuclei). **(B)** Confocal images of transition zone nuclei expressing EmGFP::SYP-3
296 and NUCL-1::mKate2 48 hours post RNAi knockdown of a non-target locus (*wrmScarlet*), *nucl-1*, *grwd-*
297 *1*, *rpoa-2*, and *fib-1* (top), as well as zoomed-in nuclei from each condition (bottom). Scale bar = 5 µm
298 (transition zone) and 0.5 µm (zoomed-in nuclei). All images were taken with identical laser intensity; due
299 to decreased SYP-3 expression under knockdown of *grwd-1, rpoa-2,* and *fib-1*, we have increased the
300 brightness of these conditions to be more comparable to wild type.

Supplementary Figure 3

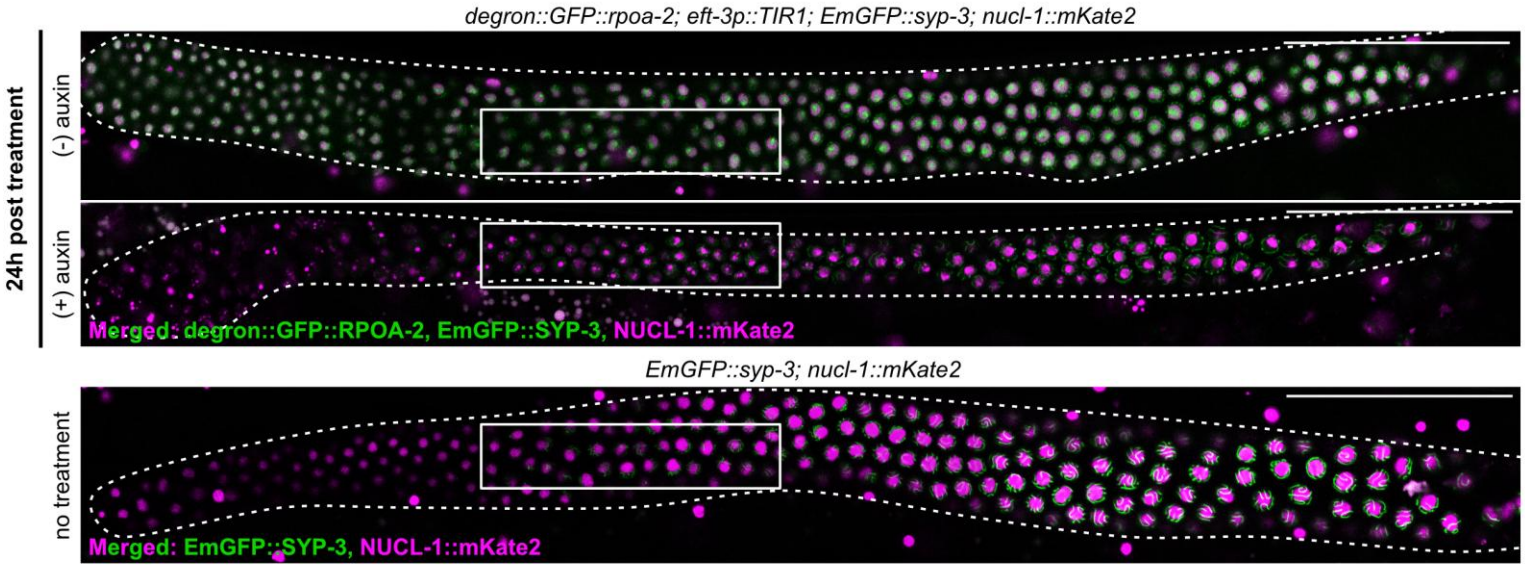

301

302 **Figure S3, Related to Figure 3. Synaptonemal complex formation under reduced Pol I activity**
303 **during the mitotic-to-meiotic transition in an adult germ line.**

304 Confocal images of adult distal germline arms (dotted lines) expressing degron::GFP::RPOA-2,
305 EmGFP::SYP-3, and NUCL-1::mKate2 following control or auxin-inducible depletion of RPOA-2 (top
306 rows). Additionally, we show a non-treated control in a wild-type genetic background (bottom row). White
307 rectangles show zoomed-in transition zone regions in **Figure 3A**. Scale bar = 50 µm.

Supplementary Figure 4

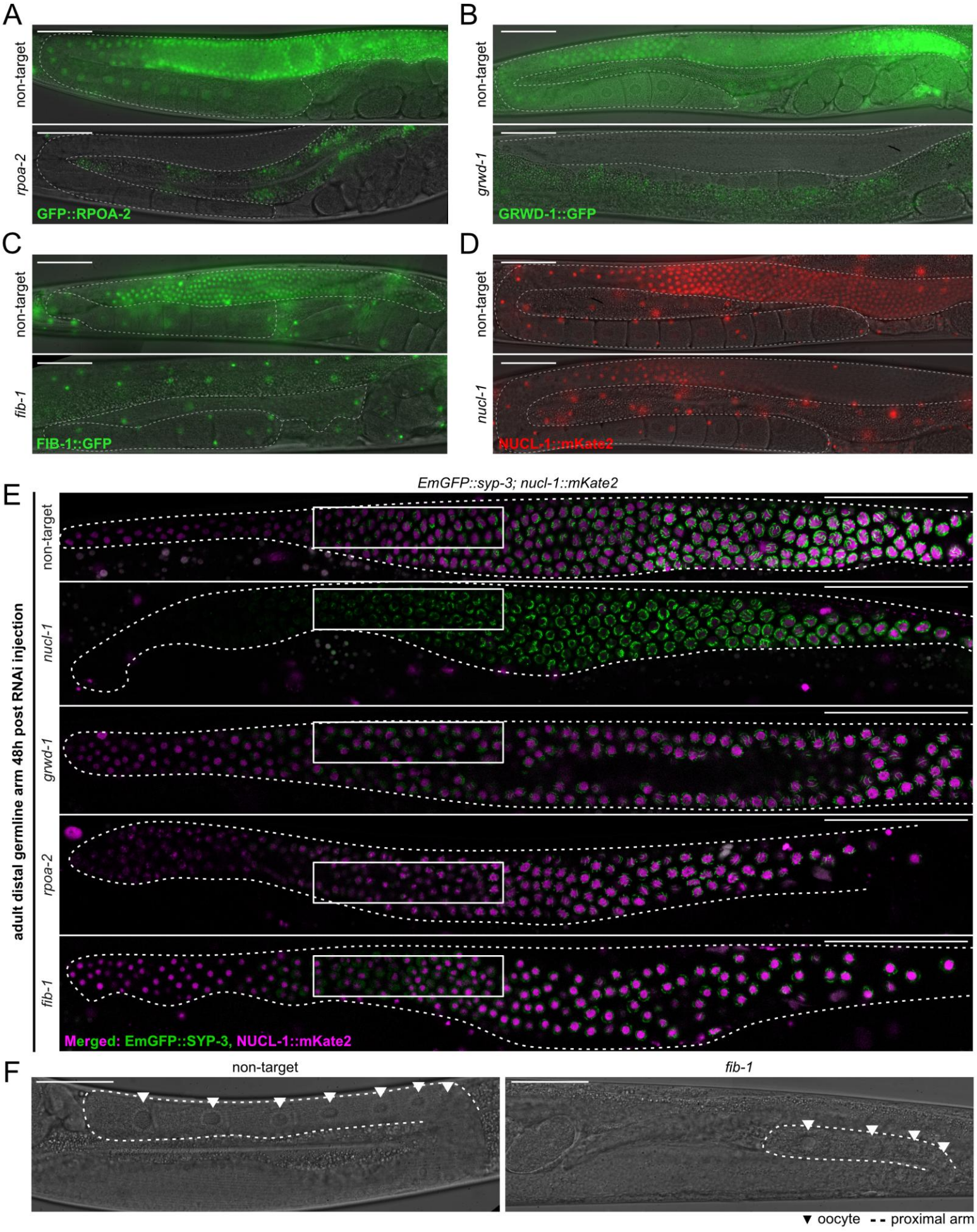

309 **Figure S4, Related to Figure 3. Examining germline synapsis and proximal oocytes after**
310 **knockdown of nucleolar proteins.**
311 **(A-D)** Merged fluorescent and DIC images of germ lines (outlined in white) after RNAi injection targeting
312 *rpoa-2* **(A)**, *grwd-1* **(B)**, *fib-1* **(C)**, and *nucl-1* **(D)**, as well as non-target (*wrmScarlet*) injection controls.
313 Each of the endogenous fluorescent-tagged proteins of the RNAi target genes show reduced germline
314 expression after 48 hours. Scale bar = 50 µm. **(E)** Confocal images of adult distal germline arms expressing
315 EmGFP::SYP-3 and NUCL-1::mKate2 48 hours post RNAi knockdown of a non-target locus (*wrmScarlet*),
316 *nucl-1*, *grwd-1*, *rpoa-2*, and *fib-1*. White rectangles show zoomed-in transition zone regions in **Figure 3B**.
317 Scale bar = 50 µm. All images were taken with identical laser intensity; due to decreased SYP-3 expression
318 under knockdown of *grwd-1, rpoa-2,* and *fib-1*, we have increased the brightness of these conditions to be
319 more comparable to wild type. **(F)** DIC images of adult proximal germline arms (dotted line) and proximal
320 oocytes (triangles) 48 hours post RNAi knockdown of a non-target locus (*wrmScarlet*) and *fib-1*. Scale bar
321 = 50 µm.

322 **Autosomal oogenesis gene promoters are more accessible after RNA Pol I depletion**

323 Given that RNA Pol I levels were associated with germline chromosome abnormalities, we next
324 investigated whether specific genomic regions were preferentially affected by a reduction of RNA Pol I
325 activity compared to reduced ribosome assembly. We performed ATAC-seq on dissected gonads from
326 control and RPOA-2- and GRWD-1-depleted young adults. In RPOA-2-depleted germ lines, 1,616 genomic
327 regions were significantly more accessible (SMA), whereas only 99 regions were significantly less
328 accessible (DESeq2, Benjamini-Hochberg adjusted $p < 0.05$). In GRWD-1-depleted germ lines, 53 regions
329 were more accessible and only one region showed reduced accessibility (DESeq2, Benjamini-Hochberg
330 adjusted $p < 0.05$). Additionally, 41 regions were SMA in both RPOA-2- and GRWD-1-depleted gonads
331 (**Figure 4A**).

332 To functionally interpret these changes, we annotated each ATAC-seq peak to its nearest genomic feature
333 and found that more than 80% of SMA peaks in either RPOA-2- or GRWD-1-depleted germ lines were
334 located within 1 kb of the promoter of the nearest gene, compared to only 50% in background peaks (**Figure**
335 **4B**). Moreover, SMA regions in RPOA-2-depleted germ lines were concentrated on autosomes (**Figure**
336 **4C**), with ~2-7% of peaks per autosome showing increased accessibility, compared to only ~0.2% on the
337 X chromosome (**Figure 4C**). In GRWD-1-depleted germ lines, SMA regions on the X chromosome were
338 also less prominent, though to a lesser extent (**Figure S5A**). Overall, these results indicate that nucleolar
339 disruption caused by reduced RNA Pol I activity leads to a more pronounced increase in chromatin
340 accessibility at autosomal promoters, emphasizing the role of nucleolar integrity in genome organization.

Figure 4

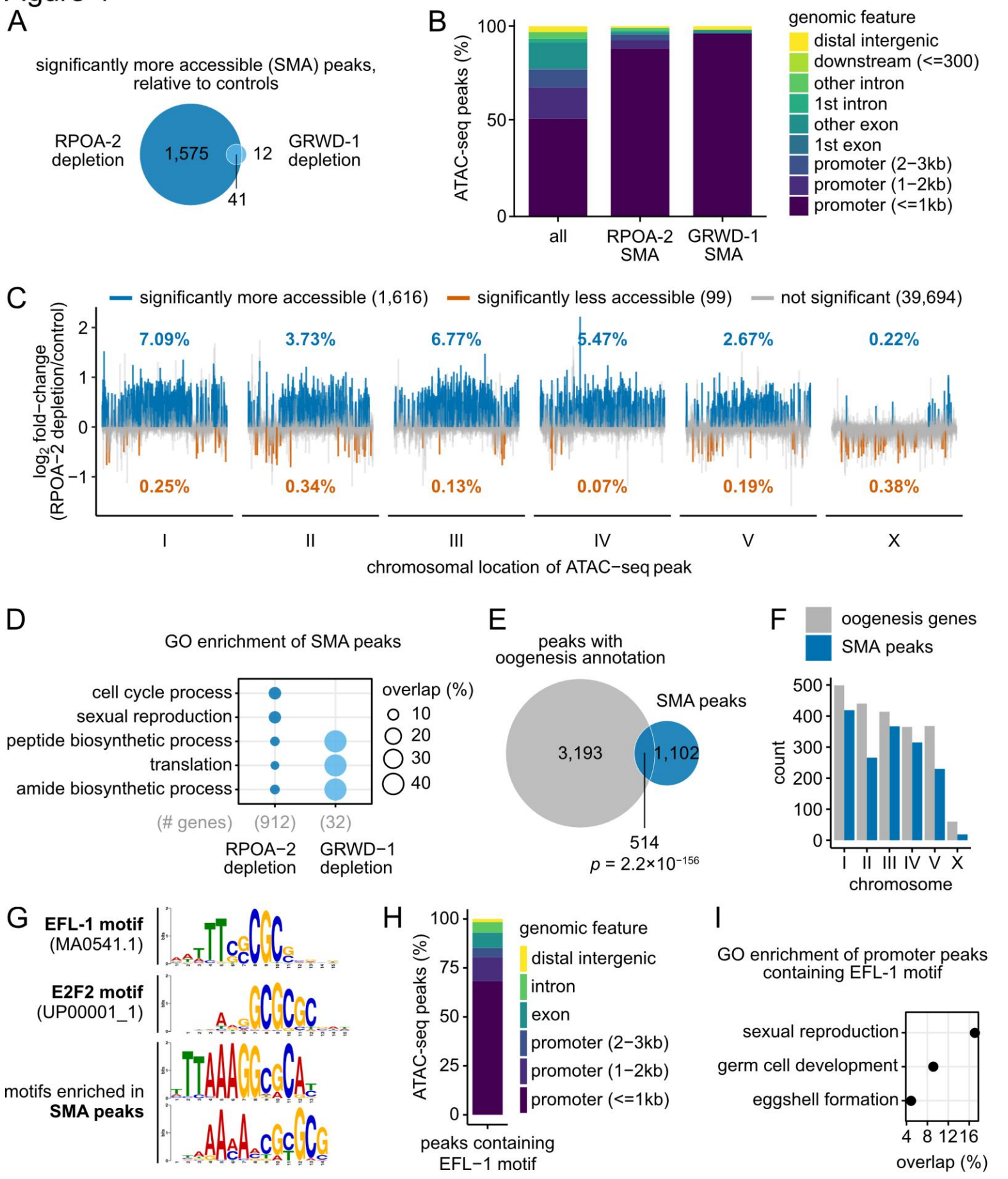
A
significantly more accessible (SMA) peaks, relative to controls
RPOA-2 depletion
1,575
12
41
GRWD-1 depletion
B
ATAC-seq peaks (%)
100
50
0
all
RPOA-2 SMA
GRWD-1 SMA
genomic feature
distal intergenic
downstream (<=300)
other intron
1st intron
other exon
1st exon
promoter (2−3kb)
promoter (1−2kb)
promoter (<=1kb)
C
significantly more accessible (1,616)
significantly less accessible (99)
not significant (39,694)
log2 fold−change (RPOA−2 depletion/control)
7.09%
3.73%
6.77%
5.47%
2.67%
0.22%
0.25%
0.34%
0.13%
0.07%
0.19%
0.38%
I
II
III
IV
V
X
chromosomal location of ATAC−seq peak
D
GO enrichment of SMA peaks
cell cycle process
sexual reproduction
peptide biosynthetic process
translation
amide biosynthetic process
overlap (%)
10
20
30
40
(# genes)
(912)
(32)
RPOA−2 depletion
GRWD−1 depletion
E
peaks with oogenesis annotation
SMA peaks
3,193
1,102
514
p = 2.2×10−156
F
oogenesis genes
SMA peaks
count
500
400
300
200
100
0
I
II
III
IV
V
X
chromosome
G
EFL-1 motif (MA0541.1)
E2F2 motif (UP00001_1)
motifs enriched in SMA peaks
H
ATAC-seq peaks (%)
100
75
50
25
0
genomic feature
distal intergenic
intron
exon
promoter (2−3kb)
promoter (1−2kb)
promoter (<=1kb)
peaks containing EFL−1 motif
I
GO enrichment of promoter peaks containing EFL-1 motif
sexual reproduction
germ cell development
eggshell formation
4
8
12
16
overlap (%)

342 **Figure 4. Disrupting RNA Pol I activity prematurely primes autosomal promoters in an accessible**
343 **state associated with oogenesis. See also Figure S5.**

344 (**A**) Venn diagram comparing the number of significantly more accessible (SMA) regions following RPOA-
345 2 depletion versus GRWD-1 depletion, based on an adjusted $p < 0.05$. (**B**) Genomic feature annotations of
346 ATAC-seq peaks. SMA regions after RPOA-2 or GRWD-1 depletion are predominantly located within 1
347 kb of the nearest promoter. (**C**) Log_2 fold-change estimates of chromatin accessibility based on gonadal
348 ATAC-seq data from at least three biological replicates per condition, each composed of 20 gonads. Each
349 segment along the x-axis represents a genomic region. The number of differentially accessible regions are
350 noted in the plot legend based on an adjusted $p < 0.05$. Percentages represent the proportion of differentially
351 accessible peaks relative to the total number of called peaks per chromosome. (**D**) Enrichment of gene
352 ontology (GO) biological processes in genes exhibiting increased accessibility after depletion of RPOA-2
353 or GRWD-1 (Hypergeometric test, FDR < 0.001). The term "gene" refers to those associated with the
354 nearest genomic feature annotation of each peak. (**E**) Overlap between peaks that are SMA after RPOA-2
355 depletion and peaks near genes involved in oogenesis [53] (Hypergeometric test). (**F**) Chromosomal
356 distribution of genes involved in oogenesis [53] and SMA peaks after RPOA-2 depletion. (**G**) Alignment of
357 the *C. elegans* EFL-1-binding site, human E2F-binding site, and the two motifs enriched in SMA peaks
358 after RPOA-2 depletion. (**H**) Genomic feature annotations of peaks containing an EFL-1-binding site. (**I**)
359 GO enrichment analysis for biological processes among genes with promoter peaks that contain an EFL-1-
360 binding site (Hypergeometric test, FDR < 0.05).

361 **RNA Pol I-driven nucleolar disruption prematurely primes oogenesis promoters in an accessible state**

362 Considering that RNA Pol I levels were linked to increased chromatin accessibility along the promoters of
363 autosomal genes, we asked whether the genes affected by these accessibility changes contribute to the
364 defective oocyte maturation that emerges specifically under reduced RNA Pol I activity. To examine this,
365 we performed a differential gene ontology (GO) analysis of biological processes enriched in genes with
366 increased accessibility following RPOA-2 or GRWD-1 depletion. Regions with increased accessibility
367 following a reduction of RNA Pol I activity were enriched for sexual reproduction and cell cycle processes,
368 including meiotic cell cycle, chromosome organization, and oogenesis (**Figure 4D** and **Table S2**,
369 Hypergeometric test, FDR < 0.001). Additionally, RPOA-2 depletion uniquely increased the accessibility
370 of genes that function both in germ/oocyte development and translation (e.g., *daz-1, fbf-2, fog-1, gld-1*, *glp-*
371 *4*, *larp-1, mex-3, oma-1*, *oma-2*) (**Figure 4D** and **Table S2**, Hypergeometric test, FDR < 0.001). In contrast,
372 depleting GRWD-1, which impairs ribosome assembly without disrupting spherical nucleolar structure, did
373 not show enrichment of sexual reproduction processes in more accessible chromatin regions. Instead, genes
374 related to translation, mostly consisting of ribosomal protein genes, mitochondrial-ribosome-related genes,
375 and translation initiation/termination factors (e.g., *rps-0, rps-9, rps-17, rps-27, rpl-9, rpl-18, rpl-25.2, rpl-*
376 *28, inf-1, larp-5, rack-1, W01D2.1*) showed increased accessibility under both RPOA-2 and GRWD-1
377 depletion, consistent with adaptive response to reduced ribosome production. These results suggest that
378 although decreased ribosome production increases accessibility at translation related loci in both conditions,
379 reducing RNA Pol I activity uniquely increases the accessibility of oogenesis genes, potentially contributing
380 to the defective oogenesis phenotype (**Figure 2**).

381 We further investigated the extent to which oogenesis genes were affected by RNA Pol I depletion using a
382 set of 2,177 genes with germline-enriched expression in feminized *fem-1(lf)* mutants [53]. Of the 3,707 peaks
383 annotated to these oogenesis genes, we detected a significant enrichment within regions that became
384 significantly more accessible after RPOA-2 depletion (**Figure 4E**, Hypergeometric test, $p = 2.2\times10^{-156}$).
385 Consistent with this observation, the autosomal bias of oogenesis genes parallels the autosomal bias in
386 accessibility observed for RPOA-2-depleted gonads (**Figure 4F**).

387 To assess potential regulators of these accessibility changes, we searched for enriched transcription factor
388 (TF) binding motifs that gained accessibility after RPOA-2 depletion. Compared to ungapped sequence
389 motifs present in background peaks, we identified eight motifs significantly enriched in the accessible peaks
390 of RPOA-2-depleted germ cells (**Table S3**, STREME, $p < 0.05$, $E < 0.05$). We aligned the eight motifs
391 enriched in RPOA-2-depleted germ lines against the 842 TF motifs present in the TFBSshape database and

392 identified 143 unique TF binding motif matches in peaks with increased accessibility after RPOA-2
393 depletion (Tomtom, $p < 0.05$, $E < 8.42$) [54]. After manual curation to combine redundant query motifs and
394 their repeated matches, we found relatively few matches with visibly cohesive alignments to their query
395 motifs. Notably, we identified four total hits to human E2F-binding sites from the enriched
396 RTGCGCCTTTAAA and CGCRCGKTKTTTRN motifs (**Figure 4G**, **Table S3**), which are orthologs to
397 the oogenesis-promoting *C. elegans* transcription factor EFL-1 [55]. Additionally, the CGCRCGKTKTTTRN
398 motif aligned to the yeast Rsc3- and Rsc30-binding sites, which regulate ribosomal protein gene expression
399 [56].

400 Although there was no enrichment of motifs for accessible regions following GRWD-1 depletion, we
401 corroborated that the EFL-1-like binding motif was specifically more accessible following RPOA-2
402 depletion, but not after GRWD-1 depletion. We identified 242 ATAC-seq peaks containing a significant
403 match to the EFL-1 motif, predominantly in promoters less than 1 kb from the nearest gene (**Figure 4H**,
404 FIMO, $p < 0.0001$). Genes with promoter peaks containing an EFL-1 motif are involved in processes such
405 as sexual reproduction, germ cell development, and eggshell formation (**Figure 4I**, Hypergeometric test,
406 FDR < 0.05). Lastly, genes with a promoter peak containing the EFL-1 motif were not remodeled after
407 reducing ribosome assembly but did show increased accessibility after reducing RNA Pol I activity (**Figure**
408 **S5F**).

409 We next examined whether these accessibility changes affected steady-state transcript levels by analyzing
410 RNA-seq data from dissected gonads after RPOA-2 or GRWD-1-depletion. We identified 188 genes with
411 increased mRNA levels and 177 genes with reduced mRNA levels upon RPOA-2 depletion (**Figure S5B**,
412 Benjamini-Hochberg adjusted $p < 0.05$). Similarly, GRWD-1 depletion led to increased mRNA levels in
413 287 genes and decreased levels in 235 genes (**Figure S5B**, Benjamini-Hochberg adjusted $p < 0.05$). We did
414 not observe significant functional GO enrichment in the over-expressed genes unique to RPOA-2 depletion
415 (**Table S5**, Hypergeometric test, FDR < 0.001). Both conditions shared 57 over-expressed genes and 87
416 under-expressed genes with a shared enrichment of under-expressed genes related to translation (**Figure**
417 **S3C-D**, Hypergeometric test, FDR < 0.001), mirroring patterns observed in chromatin accessibility.
418 Moreover, we found no overall correlation between chromatin accessibility and mRNA levels for all genes
419 or for those that were differentially accessible and differentially expressed (**Figure S5E**, $p > 0.05$).

420 Given the enrichment of a putative repressive Rsc30-like motif in accessible regions following RPOA-2
421 depletion, we hypothesized that translation-related genes would be under-expressed. Indeed, many
422 ribosomal protein genes are significantly reduced after RPOA-2 depletion, consistent with negative

423 regulation (**Figure S5G**, one-tailed one-sample *t*-test, alternative hypothesis: average $\log_2$ fold-change < 0,
424 $p = 0.00020$). Such coordinated repression can be explained by previously described feedback mechanisms
425 that couple ribosomal protein gene expression directly to rRNA transcription. Specifically, the
426 transcriptional activator Ifh1 interacts with the rRNA processing factor Utp22 to synchronize ribosomal
427 protein gene transcription with rRNA synthesis [57]. Under conditions of impaired rRNA synthesis, as occurs
428 with RPOA-2 depletion, Utp22 is no longer sequestered by rRNA and thus becomes available to bind
429 ribosomal protein gene promoters, leading to transcriptional repression. In contrast, depletion of GRWD-1
430 disrupts assembly of the 60S ribosomal subunit without directly impairing rRNA transcription (**Figure 1F,**
431 **S1C, S1D**). As a result, the Utp22-mediated feedback inhibition of ribosomal protein genes is likely not
432 triggered, and instead these genes become overexpressed as a compensatory response to defective ribosome
433 assembly (**Figure S5D**).

434 In contrast, genes related to sexual reproduction did not exhibit increased transcript levels, despite increased
435 chromatin accessibility and the enrichment of a potential oogenesis-promoting transcription factor motif
436 (**Figure S5G**, one-tailed one-sample *t*-test, alternative hypothesis: average $\log_2$ fold-change > 0, $p = 0.16$).
437 In agreement, genes with a promoter peak containing an EFL-1 motif did not significantly increase mRNA
438 expression after RPOA-2 depletion (**Figure S5F**, one-tailed one-sample *t*-test, alternative hypothesis: $\log_2$
439 fold-change > 0, $p = 0.14$). Thus, although oogenesis promoters become more accessible, mRNA levels
440 remain unchanged, reflecting an oogenesis-specific chromatin state that is primed for but does not undergo
441 productive transcription.

442 Together, these results suggest that decreasing RNA Pol I activity triggers nucleosome remodeling to reduce
443 the expression of ribosomal proteins, potentially conserving resources in response to limited rRNA
444 availability for ribosome biogenesis. However, this reduction in RNA Pol I activity also leads to
445 nucleosome remodeling that increases the accessibility of oogenesis-related genes and oogenesis-promoting
446 EFL-1 binding sites, potentially contributing to a defective oocyte maturation phenotype (**Figure 2**).

Supplementary Figure 5

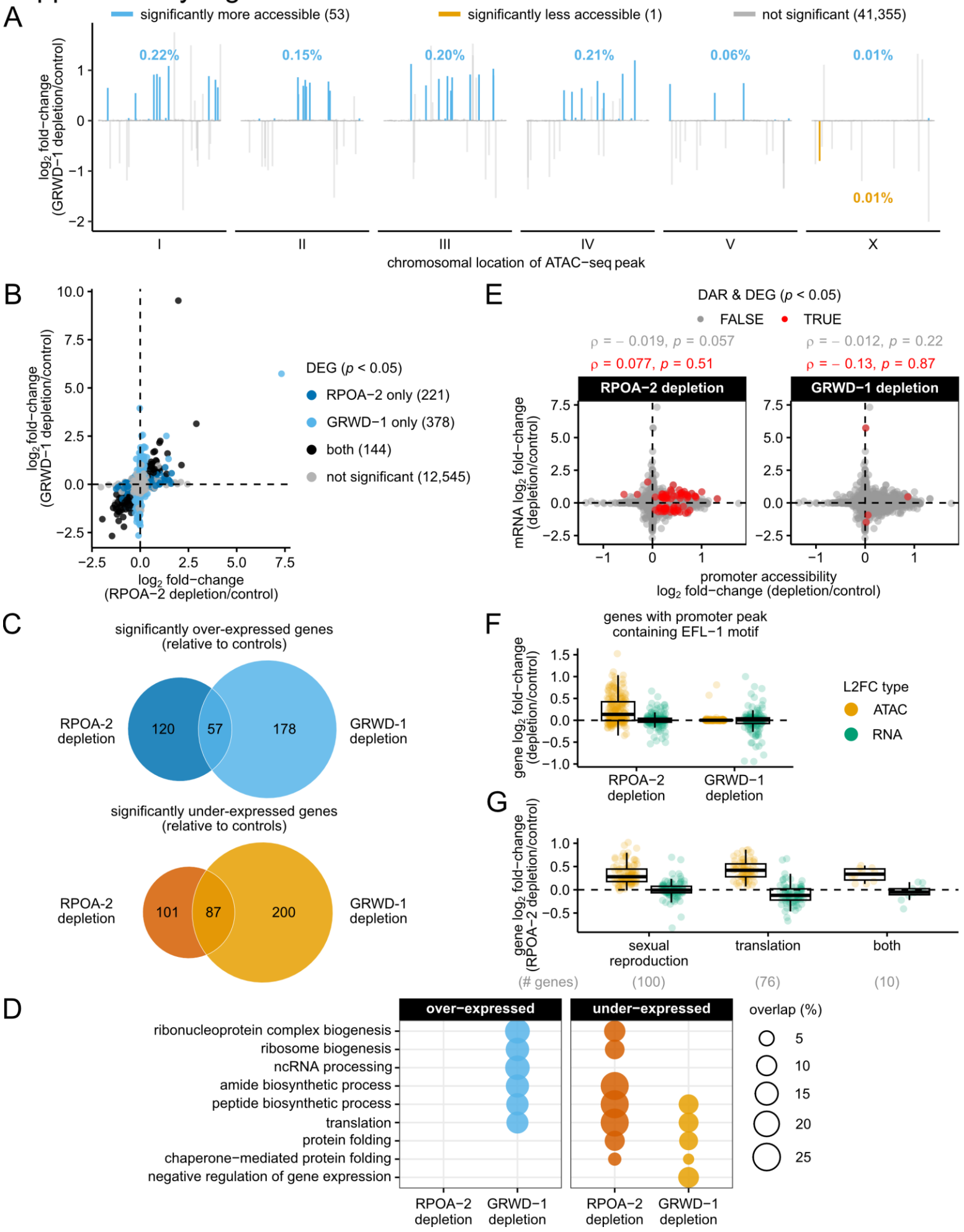

448 **Figure S5, Related to Figure 4. Effects of RPOA-2 and GRWD-1 depletion on germline chromatin**
449 **accessibility and gene expression.**

450 (**A**) Log_2 fold-change estimates of chromatin accessibility based on gonadal ATAC-seq data from at least
451 three biological replicates per condition, each composed of 20 gonads. Each segment along the x-axis
452 represents a genomic region. The number of differentially accessible regions are noted in the plot legend
453 based on an adjusted $p < 0.05$. Percentages represent the proportion of differentially accessible peaks
454 relative to the total number of called peaks per chromosome. (**B**) Log_2 fold-change estimates of gene
455 expression from RNA-seq conducted on dissected gonads after RPOA-2 or GRWD-1 depletion. Biological
456 replicates, consisting of 20 gonads: RPOA-2 control = 3, RPOA-2 depletion = 4, GRWD-1 control = 2,
457 GRWD-1 depletion = 3. (**C**) Venn diagram to contextualize the difference in the scale of gene expression
458 changes after RPOA-2 depletion compared to GRWD-1 depletion. (**D**) Enrichment of gene ontology
459 biological processes in genes that were differentially expressed after RPOA-2 or GRWD-1 depletion
460 (Hypergeometric test, FDR < 0.001). (**E**) Log_2 fold-change estimates of promoter accessibility versus
461 mRNA to investigate whether chromatin accessibility correlated with gene expression. We did not identify
462 a significant correlation between promoter accessibility and mRNA levels across all genes (gray), or across
463 genes that were both differentially accessible and differentially expressed after RPOA-2 or GRWD-1
464 depletion (black). (**F**) Comparison of ATAC-seq and RNA-seq log_2 fold-change estimates for genes with
465 promoter peaks containing an EFL-1 motif after RPOA-2 or GRWD-1 depletion. On average, genes with a
466 promoter EFL-1 motif did not show a significant increase in mRNA fold-changes after RPOA-2 depletion
467 (one-tailed one-sample *t*-test, alternative hypothesis: log_2 fold-change > 0, $p = 0.14$). (**G**) Comparison of
468 ATAC-seq and RNA-seq log_2 fold-change estimates in biological processes enriched in genes with
469 increased chromatin accessibility after RPOA-2 depletion. Only the terms "sexual reproduction" and
470 "translation" are represented, as they encompass the majority of related subprocesses. "Both" represents
471 genes that are involved in both biological processes. On average, translation-related genes, including
472 ribosomal proteins, have lower mRNA fold-changes after RPOA-2 depletion (one-tailed one-sample *t*-test,
473 alternative hypothesis: average log_2 fold-change < 0, $p = 0.00020$), whereas genes related to sexual
474 reproduction do not have significantly increased mRNA levels (one-tailed one-sample *t*-test, alternative
475 hypothesis: log_2 fold-change > 0, $p = 0.16$).

476 **Increases in chromatin accessibility upon Pol I depletion are accompanied by oogenesis-specific**
477 **histone remodeling**

478 Throughout oogenesis, germ cells undergo extensive chromatin remodeling to prepare for meiotic
479 chromosome condensation and subsequent zygotic genome activation (ZGA). One hallmark of this
480 transition is the redistribution of H3K4me3 from gene bodies to promoters in mature oocytes [4]. Given that
481 RPOA-2 depletion increases the accessibility of oogenesis-related regions, we asked whether these loci
482 show typical signatures of H3K4me3 remodeling in maturing wild-type oocytes.

483 Genes undergoing H3K4me3 remodeling during oogenesis can be grouped into three clusters: Cluster 1
484 (strong H3K4me3 marks in both promoters and gene bodies), Cluster 2 (strong promoter-specific
485 H3K4me3), and Cluster 3 (weaker promoter-specific H3K4me3) [4]. When we compared chromatin
486 accessibility near genes in these clusters, we found that accessibility near oogenesis-specific H3K4me3
487 remodeled genes significantly increased after RPOA-2 depletion relative to a random set of regions (**Figure**
488 **5A**, Bonferroni-corrected one-tailed Welch's two-sample *t*-tests, $p < 0.05$). Consistent with the germ-to-
489 oocyte H3K4me3 remodeling pattern, Cluster 1 genes showed increased chromatin accessibility along both
490 promoters and gene bodies (**Figure 5B**, top). Cluster 2 genes exhibited increased accessibility mainly in
491 promoters, while Cluster 3 genes displayed weaker promoter specific increases following RPOA-2
492 depletion (**Figure 5B**, middle and bottom).

493 Although reducing RNA Pol I activity shows signatures of H3K4me3 remodeling, changes in chromatin
494 accessibility can also reflect the remodeling of other histone marks. We compared the abundance of three
495 such histone marks—remodeled active H3K4me3, non-remodeled active H3K36me3, and non-remodeled
496 repressive H3K27me3—within regions that became more accessible after RPOA-2 depletion, using
497 available ChIP-seq data from wild-type germ cells and oocytes [58–60]. In wild-type germ cells, H3K27me3
498 marks were less abundant in SMA regions compared to random regions (**Figure 5C**, top left), while active
499 marks (H3K36me3 and H3K4me3) were enriched in SMA regions (**Figure 5C**, top middle and right). In
500 wild-type oocytes, we expected highly accessible regions after RPOA-2 depletion to show specific
501 enrichment for H3K4me3, reflecting germ-to-oocyte histone remodeling. In agreement, H3K4me3 marks
502 were enriched in SMA regions relative to random regions (**Figure 5C**, bottom right), while H3K27me3 and
503 H3K36me3 signals were weak in both accessible and random regions (**Figure 5C**, bottom left and middle).

504 Since more than 80% of SMA peaks are near promoters (**Figure 4B**), and H3K4me3 marks shift to
505 promoters in oocytes, we hypothesized that H3K4me3 signal would peak at the center of SMA regions in
506 wild-type oocytes. In contrast, we expected H3K4me3 in wild-type germ cells to decrease around SMA

507 regions, since H3K4me3 is typically present along gene bodies in germ cells. This pattern was confirmed,
508 with H3K4me3 signal peaking in SMA regions relative to a random set of promoters in wild-type oocytes
509 (**Figure 5D**, right) and decreasing around SMA regions in wild-type germ cells. H3K27me3 and
510 H3K36me3 signals did not notably peak near SMA regions in either germ cells or oocytes (**Figure 5D**, left
511 and middle). Our findings support that reducing RNA Pol I activity throughout the germ line specifically
512 increases the accessibility of promoters that are remodeled during the germ-to-oocyte transition through
513 H3K4me3 deposition, suggesting that the spatiotemporal regulation of H3K4 methylation is misregulated
514 under RNA Pol I-mediated nucleolar disruption.

515 In wild-type animals, H3K4 methylation progressively increases towards the proximal region of the gonad,
516 and this spatial regulation of H3K4 methylation is essential for proper germ line maturation [12,61]. Given that
517 RPOA-2 depletion increases the accessibility of oogenesis-associated H3K4me3 regions and specifically
518 disrupts oogenesis, we anticipated that the spatial regulation of H3K4 methylation would be altered in
519 response to RPOA-2 depletion, likely through premature H3K4me3 deposition in accordance with
520 increased chromatin accessibility. To investigate this, we performed gonadal H3K4me3 immunostaining
521 and cell-segmentation image analysis to assess how reduced RNA Pol I activity affects changes in the
522 deposition of H3K4me3 from the distal to proximal end of the gonad (**Figure 5E**, n = 50 control gonads
523 with 3,933 cells, n = 77 depletion gonads with 8,134 cells). Individual germ cell positions were projected
524 onto a linear gonad axis to evaluate how H3K4me3 immunostaining intensity correlated with cell position
525 along the distal-proximal gonad axis (termed cell gonad position from here on) (**Figure 5F**, see Methods).

526 As expected, an aggregate analysis of cells from all control gonads revealed a significant gradual increase
527 in H3K4 methylation along the distal-proximal axis, evidenced both by H3K4me3/DAPI normalized
528 intensity (**Figure 5G, top**, Spearman coefficient = 0.41) and by per-gonad scaled H3K4me3 intensity
529 (**Figure 5G, bottom**, Spearman coefficient = 0.36). Similarly, we also analyzed this positive H3K4me3
530 gradient within individual gonads and observed that the majority (84%) of control gonads had significant
531 correlations between cell gonad position and normalized H3K4me3/DAPI intensity (**Figure 5H**, mean
532 Spearman coefficient: 0.46±0.03, Benjamini-Hochberg adjusted p-value < 0.05), and also per-gonad scaled
533 H3K4me3 intensity (**Figure 5H**, mean Spearman coefficient: 0.36±0.03, 78% with Benjamini-Hochberg
534 adjusted p-value < 0.05). These results support that typical oogenesis is consistently associated with a
535 moderate but important positive H3K4me3 gradient.

536 Under reduced RNA Pol I activity, the aggregated correlation between cell gonad position and H3K4me3
537 was reduced by approximately half, both relative to normalized H3K4me3/DAPI and per-gonad scaled

538 H3K4me3 intensity (**Figure 5G**, Spearman coefficient = 0.26 and 0.14 for H3K4me3/DAPI and per-gonad
539 scaled H3K4me3, respectively). Additionally, only 64% of RPOA-2-depleted gonads had significant, but
540 weaker, correlations between cell gonad position and normalized H3K4me3/DAPI intensity (**Figure 5H**,
541 mean Spearman coefficient: 0.23±0.04, Benjamini-Hochberg adjusted p-value < 0.05) and also per-gonad
542 scaled H3K4me3 intensity (**Figure 5H**, mean Spearman coefficient: 0.12±0.03, 52% with Benjamini-
543 Hochberg adjusted p-value < 0.05).

544 Lastly, compared to control gonads, RPOA-2-depleted gonads had a significant reduction in average
545 correlation between cell gonad position and H3K4me3 (**Figure 5H**, one-tailed Welch's two-sample t-test,
546 H3K4me3/DAPI: Benjamini-Hochberg adjusted p-value = 3.0×10^{-5}, per-gonad scaled H3K4me3:
547 Benjamini-Hochberg adjusted p-value = 4.6×10^{-7}). Interestingly, this misregulation of H3K4me3
548 deposition could be explained by increased H3K4me3 in the distal region (**Figure 5G, top**).

549 Given RPOA-2 depletion specifically disrupts the spatiotemporal regulation of H3K4 methylation,
550 premature and aberrant deposition of H3K4me3 likely interferes with synapsis and meiotic chromosome
551 organization. Indeed, previous studies have established that disrupted H3K4 methylation dynamics strongly
552 correlate with recombination abnormalities, and defects in synaptonemal assembly and stability [62,63].
553 Consistent with these findings, we also observed synapsis defects indicated by altered SYP-3 localization,
554 following RPOA-2 depletion (**Figure 3A-B, S4**).

555 To further dissect the mechanistic basis underlying these defects, we asked whether nucleolar disruption
556 and associated chromatin alterations activate the meiotic DNA damage checkpoint kinases ATM-1 and
557 ATL-1. Immunostaining for phosphorylated serine/threonine residues, a hallmark of ATM/ATR checkpoint
558 activation, revealed visibly increased checkpoint signaling specifically upon RPOA-2 depletion, but not
559 after GRWD-1 depletion, suggesting checkpoint activation is specific to RNA Pol I mediated nucleolar
560 stress (**Figure S6A**).

561 ATM/ATR activation is known to trigger CEP-1 (p53) mediated apoptosis in the presence of extensive
562 DNA damage or unresolved meiotic recombination intermediates. Thus, we asked whether increased
563 ATM/ATR phosphorylation following RPOA-2 depletion led to activation of CEP-1/p53. RNAi
564 experiments targeting *rpoa-2* or *grwd-1* in a CEP-1::GFP reporter strain showed no visible increase in CEP-
565 1 expression compared to control RNAi (**Figure S6B**). These data indicate that the meiotic chromosome
566 defects and associated checkpoint activation induced by RNA Pol I depletion occur independently of
567 apoptosis, consistent with acridine orange staining results, which revealed no significant increase in

568 apoptotic cells (**Figure S2A, B**). Instead, these results suggest that ATM/ATR checkpoint activation occurs
569 in conjunction with synapsis defects.

570 Given the proposed role of SET-2 (the *C. elegans* homolog of SET1 responsible for catalyzing H3K4
571 methylation) in preserving genome integrity and regulating chromatin compaction in the germ line [63,64], we
572 hypothesized that SET-2 might mediate the aberrant H3K4 methylation observed following RPOA-2
573 depletion. We further reasoned that loss of SET-2 function might rescue or alter the oogenesis defects and
574 abnormal methylation patterns seen after RPOA-2 depletion. To test this hypothesis, we crossed the *set-*
575 *2(ok592)* mutant into the RPOA-2 AID strain. However, RPOA-2 depletion in the *set-2(ok592)* mutant
576 background still resulted in a reduced number of enlarged oocytes (**Figure S6C**), indicating that SET-2
577 does not significantly influence the RNA Pol I dependent oogenesis defects. Furthermore, H3K4me3
578 immunostaining revealed persistently increased H3K4 trimethylation upon RPOA-2 depletion in the
579 absence of SET-2 function (*set-2(ok592*)), suggesting that SET-2 is not the methyltransferase responsible
580 for the aberrant methylation triggered by loss of RPOA-2 (**Figure S6D**).

581 Together, our data support a model (**Figure 6**) in which RNA Pol I–dependent nucleolar integrity is
582 essential to maintain the proper spatiotemporal regulation of H3K4 methylation during oogenesis.
583 Specifically, reducing RNA Pol I activity results in premature and ectopic deposition of H3K4me3 at the
584 promoters of oogenesis-related genes, leading to abnormal chromatin accessibility patterns. These aberrant
585 chromatin states likely interfere with synaptonemal complex formation and homologous recombination,
586 triggering sustained ATM/ATR checkpoint activation independent of CEP-1/p53 mediated apoptosis.
587 Rather than apoptosis, this checkpoint activation likely leads to meiotic cell-cycle perturbation, suggesting
588 an epigenetic feedback loop that safeguards germline genome integrity upon nucleolar disruption and
589 associated chromatin misregulation (**Figure 6**).

Figure 5

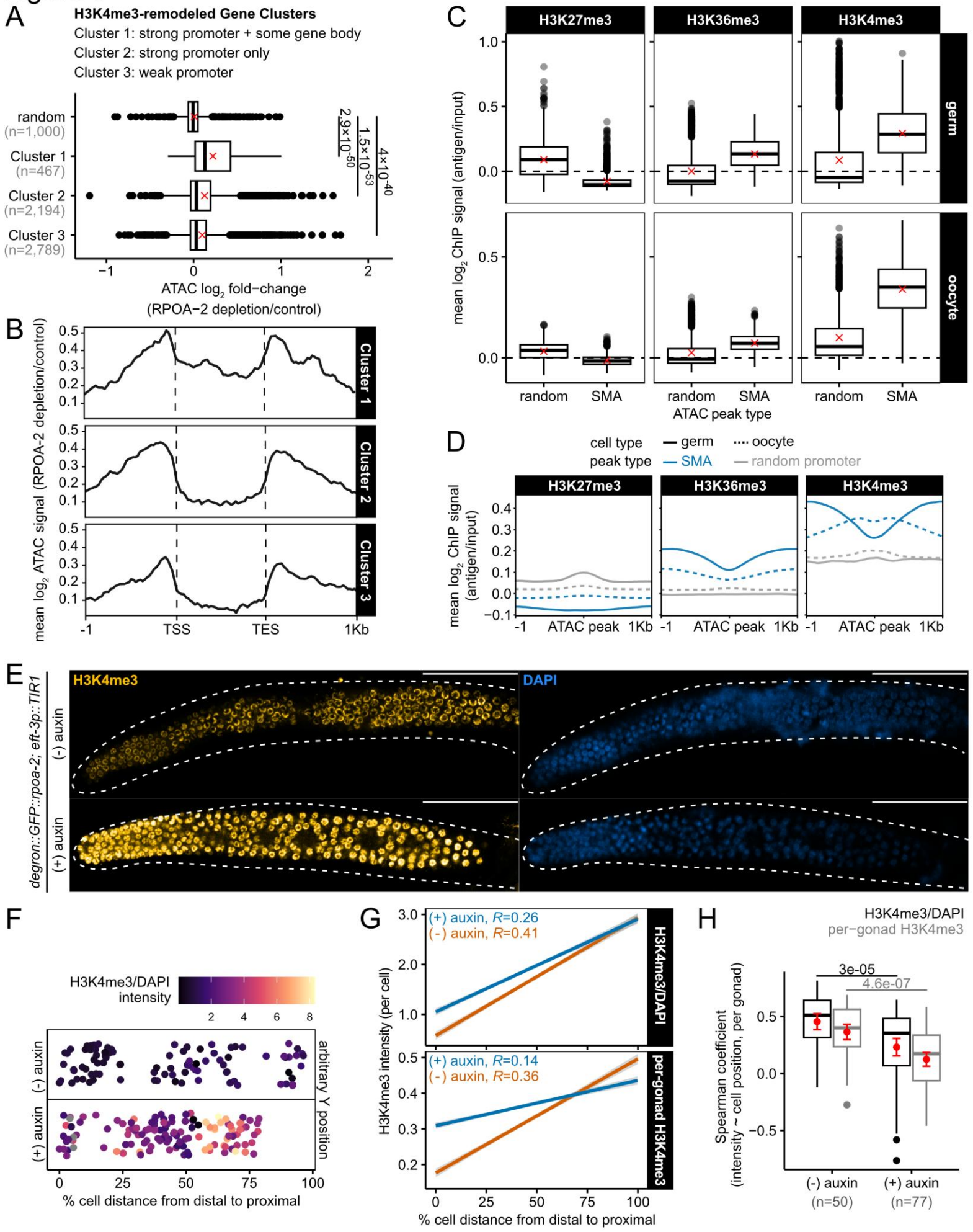
A
H3K4me3-remodeled Gene Clusters
Cluster 1: strong promoter + some gene body
Cluster 2: strong promoter only
Cluster 3: weak promoter
random (n=1,000)
Cluster 1 (n=467)
Cluster 2 (n=2,194)
Cluster 3 (n=2,789)
2.9×10^-50
1.5×10^-53
4×10^-40
ATAC log2 fold−change (RPOA−2 depletion/control)
B
mean log2 ATAC signal (RPOA-2 depletion/control)
Cluster 1
Cluster 2
Cluster 3
-1
TSS
TES
1Kb
C
H3K27me3
H3K36me3
H3K4me3
germ
oocyte
mean log2 ChIP signal (antigen/input)
random
SMA
ATAC peak type
D
cell type
germ
oocyte
peak type
SMA
random promoter
mean log2 ChIP signal (antigen/input)
ATAC peak
E
H3K4me3
DAPI
degron::GFP::rpoa-2; eft-3p::TIR1
(-) auxin
(+) auxin
F
H3K4me3/DAPI intensity
arbitrary Y position
% cell distance from distal to proximal
G
(+) auxin, R=0.26
(-) auxin, R=0.41
H3K4me3/DAPI
(+) auxin, R=0.14
(-) auxin, R=0.36
per-gonad H3K4me3
H3K4me3 intensity (per cell)
% cell distance from distal to proximal
H
H3K4me3/DAPI
per−gonad H3K4me3
3e-05
4.6e-07
Spearman coefficient (intensity ~ cell position, per gonad)
(-) auxin (n=50)
(+) auxin (n=77)

591 **Figure 5. Chromatin regions that become more accessible after reducing RNA Pol I activity display**
592 **patterns of H3K4me3 remodeling characteristic of the germ-to-oocyte transition. See also Figure S6.**

593 (**A**) Log_2 fold-change estimates of chromatin accessibility after RPOA-2 depletion in peaks annotated to
594 genes that undergo H3K4me3 remodeling during oogenesis, compared to a random subset of peaks. The
595 number of peaks in each set is specified by *n*, and means are denoted by an *x*. Statistical comparisons were
596 performed using right-tailed Welch's two-sample *t*-tests with Bonferroni corrections. (**B**) Metagene
597 analysis of mean log_2 ATAC signal (RPOA-2 depletion/control) within 1 kb of genes that undergo
598 H3K4me3 remodeling during oogenesis. In gonads with reduced RNA Pol I activity, the shape of chromatin
599 accessibility signal within each cluster mirrors the shape of H3K4me3 remodeling associated with each
600 gene cluster. (**C**) Distribution of average H3K27me3, H3K36me3, and H3K4me3 ChIP signals from wild-
601 type germ cells or oocytes within ATAC-seq peaks that are significantly more accessible (SMA) after
602 RPOA-2 depletion, compared to signals within an identically-sized random subset of regions. Means are
603 denoted by an *x*. (**D**) Metagene plot displaying the average H3K27me3, H3K36me3, and H3K4me3 ChIP
604 coverage from wild-type germ cells or oocytes within 1 kb of genomic regions that are SMA after RPOA-
605 2 depletion, compared to coverage within an identically-sized random subset of promoter ATAC-seq peaks
606 that are not SMA. (**E**) Representative 3-D confocal projections of adult gonad arms with H3K4me3
607 immunostaining and DAPI after control treatment or RPOA-2 depletion. Dotted lines represent gonad
608 boundaries determined from T-PMT. Scale bar = 50 µm. (**F**) Using the example gonads from (E), we show
609 germ cell position along a linear gonad axis following implementation of a gonad linearization algorithm
610 (see Methods). Each point represents a germ cell detection; however, note that not all gonadal cells are
611 detected by the algorithm. The distal tip is represented by zero on the gonad axis, whereas the most proximal
612 tip of the gonad is variable based on biological size, gonad disruption during immunostaining, or gonad
613 placement on Z-plane. H3K4me3 intensity measurements are normalized to DAPI to account for
614 differences in permeability across gonads. (**G**) Linear relationship between germ cell position along the
615 gonadal axis (from distal to proximal end) and H3K4me3 signal intensity (relative to DAPI intensity or
616 scaled per-gonad), aggregated across all gonads. Spearman correlation coefficients are represented on the
617 plot. Linear models and overall correlations are based on data from 3,933 control cell detections and 8,134
618 depletion cell detections from 50 and 77 gonads, respectively. (**H**) Distribution of Spearman coefficients
619 estimating per-gonad positive correlations between cell position on the gonad axis and H3K4me3 intensity
620 (relative to DAPI intensity or scaled per-gonad). Mean and standard error are represented by red points and
621 crossbars. The number of gonads analyzed per condition are represented by *n*. A one-tailed Welch's two-
622 sample *t*-test suggests that on average, control gonads have a higher magnitude correlation than gonads
623 with reduced RNA Pol I activity (Benjamini-Hochberg adjusted *p*-values).

Supplementary Figure S6

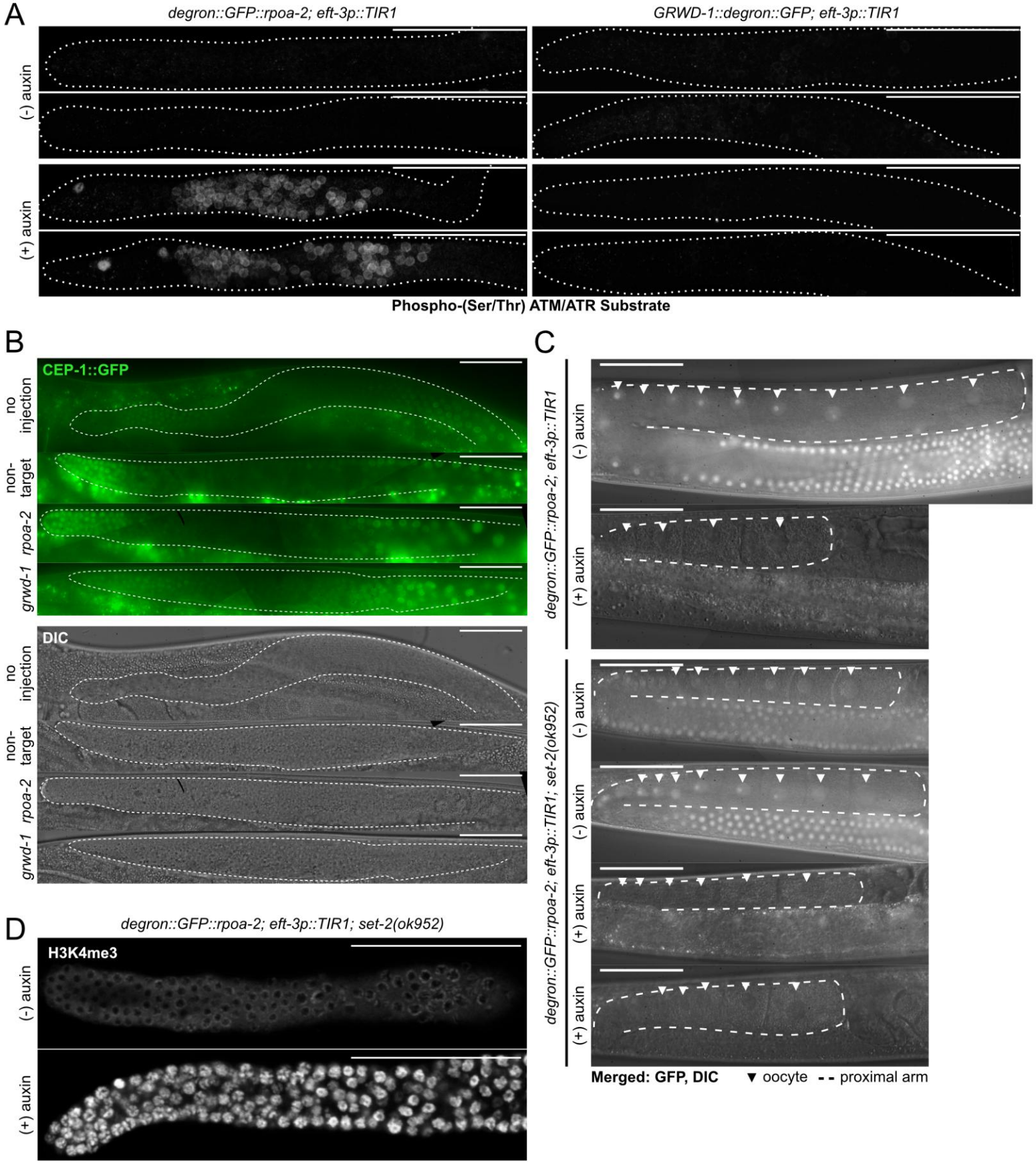

625 **Figure S6, Related to Figure 5. Pol I reduction uniquely triggers ATM/ATR signaling in a CEP-1**
626 **independent manner (A-B); H3K4 trimethylation increases under reduced Pol I activity in a SET-2**
627 **independent manner (C-D).**

628 (**A**) Average confocal projections of dissected gonad arms (outlined in white) immunostained for Phospho-
629 (Ser/Thr) ATM/ATR Substrate after auxin-inducible depletion of RPOA-2/GRWD-1. All conditions were
630 imaged with identical laser settings. Scale bar = 50 µm. (**B**) Fluorescent and DIC images of CEP-1::GFP
631 expression in the germ line (outlined in white) after RNAi injection targeting *rpoa-2* and *grwd-1*, as well
632 as non-target injection and no injection controls. All conditions imaged with identical settings. Scale bar =
633 50 µm. (**C**) Merged fluorescent (degron::GFP::RPOA-2) and DIC images of adult germ lines after auxin-
634 inducible depletion of RPOA-2 in a wild-type or *set-2(ok952)* genetic background. Dotted lines highlight
635 the proximal arm; triangles point to proximal oocytes. Scale bar = 50 µm. (**D**) Representative average
636 confocal projections of adult gonad arms that have been immunostained for H3K4me3 after auxin-inducible
637 depletion of RPOA-2 in a *set-2(ok952)* genetic background. Dotted lines represent gonad boundaries
638 determined from T-PMT. Scale bar = 50 µm.

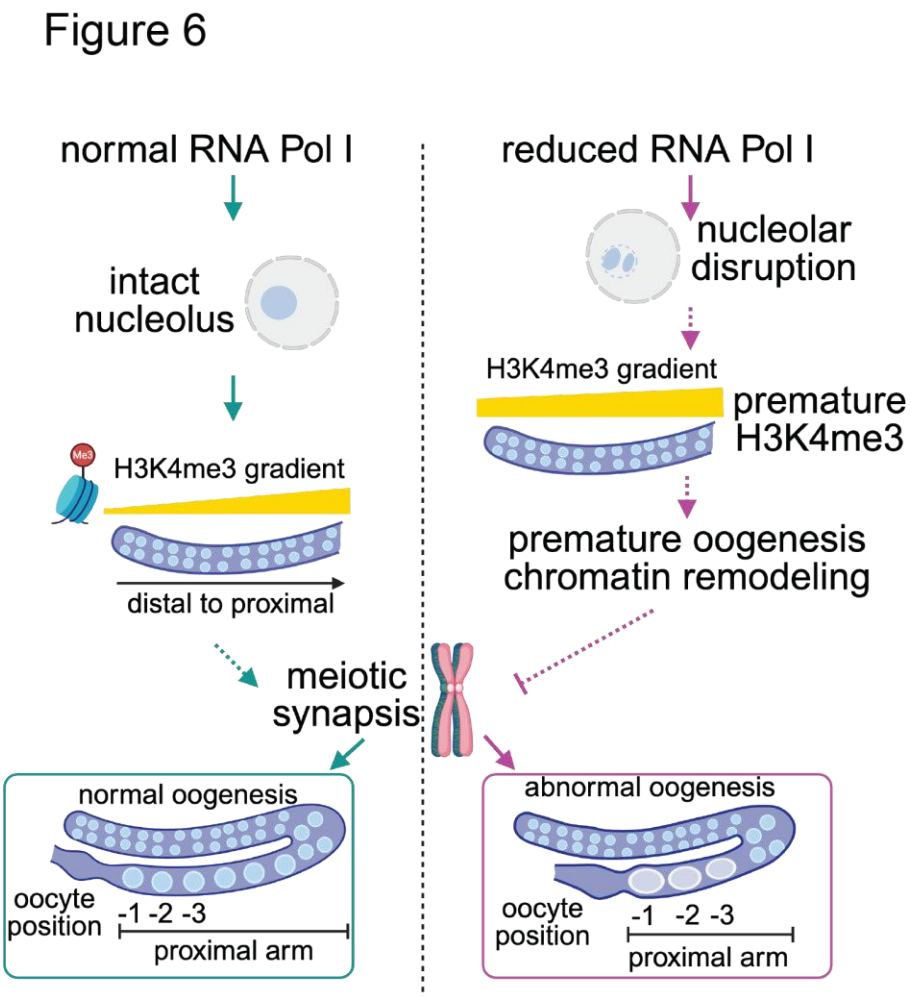

Figure 6. Schematic model illustrating the non-ribosomal function of RNA Pol I during *C. elegans* oogenesis.

Under normal conditions (left), RNA Pol I activity maintains nucleolar integrity, which supports the establishment of a proper H3K4me3 gradient from the distal to proximal germ line. This gradient facilitates meiotic synapsis and the progression of oogenesis, resulting in normal oocyte formation. When RNA Pol I activity is reduced (right), nucleolar disruption leads to premature and ectopic H3K4me3 deposition and aberrant oogenesis chromatin remodeling. This dysregulation interferes with the mitotic-to-meiotic transition, resulting in decreased synapsis that leads to abnormal oogenesis, characterized by fewer and enlarged oocytes. The model proposes an epigenetic feedback mechanism that links nucleolar function to germline genome integrity. Created in BioRender. https://BioRender.com/oq1fz8k.

650 **DISCUSSION**

651 In this study, we investigated non-ribosomal functions of the nucleolus during oogenesis using separation-
652 of-function strains in *Caenorhabditis elegans*. By leveraging the auxin-inducible degron (AID) system, we
653 selectively depleted catalytic subunits of RNA Polymerase I (RPOA-1 and RPOA-2) and two ribosome
654 assembly factors (GRWD-1 and TSR-2) in the germ line. This approach enabled us to distinguish between
655 the effects of nucleolar disruption and reduced ribosome biogenesis, revealing that germ cell nucleoli
656 actively regulate meiotic progression through epigenetic mechanisms independent of ribosome production.
657 Our findings uncover a previously unrecognized role for RNA Pol I activity and nucleolar integrity in
658 oogenesis beyond ribosome production.

659 **Differential impacts of nucleolar versus ribosomal stress on oogenesis and meiotic synapsis**

660 A key insight from our work is the distinct impact of nucleolar versus ribosomal stress on germ cell
661 differentiation. Near-complete reduction of ribosome assembly had minimal consequences for oocyte
662 production (**Figure 2**), suggesting that the oogenesis program, including meiotic synapsis and histone
663 remodeling, is not heavily dependent on ribosome biogenesis (**Figure 3-4**). In contrast, disruption of
664 nucleolar structure through near-complete reduction of RNA Pol I activity leads to significant oogenesis
665 and synapsis defects (**Figure 2-3**). These results suggest that nucleolar integrity, rather than downstream
666 capacity for protein synthesis, is essential for proper germ cell progression through oogenesis.

667 Our previous work highlights the importance of ribosome loading in maturing oocytes to support
668 embryogenesis in *C. elegans* [22]. However, our current results show that ribosome biogenesis is not critical
669 for oogenesis itself, at least within the timeframe of our investigation. Furthermore, we previously
670 demonstrated that somatic chromatin reorganization and developmental progression beyond the L2 stage
671 are similarly affected by either nucleolar or ribosomal stress, indicating a uniform response in somatic
672 tissues [43,65]. Here, however, germ cells entering meiosis exhibit a unique sensitivity to nucleolar disruption,
673 suggesting that meiotic cells, with their distinct chromatin remodeling requirements, are particularly
674 vulnerable to changes in nucleolar homeostasis.

675 One explanation may be that meiotic germ cells, which are relatively quiescent in their transcription and
676 translation activities, do not strongly depend on ongoing ribosome production. However, their reliance on
677 large–scale chromosome restructuring places them at risk when nucleolar integrity is compromised; several
678 lines of evidence in other organisms and tissues suggest that nucleolar integrity is linked to genome
679 organization and stress sensing [66–71]. In female gametogenesis in particular, intact nucleolar structure has

680 been shown to have several implications for successful oogenesis unrelated to ribosome production. These
681 functions include safeguarding genomic stability by shielding repetitive rDNA loci from recombination,
682 preserving satellite repeat sequences, and sequestering transcriptional silencing factors, all of which are
683 crucial for successful oogenesis [23–25]. Thus, given the potential consequences of aberrant nucleolar structure
684 in maturing germ cells, it is likely that nucleolar stress-sensing mechanisms play a role in regulating meiotic
685 progression.

686 In support of this view, reductions in ribosome assembly, which maintains a spherical nucleolar structure,
687 does not noticeably impair the mitotic-to-meiotic transition as assessed by SYP-3 localization in the
688 transition zone and pachytene stages (**Figure 3**). In contrast, depletion of RNA Pol I activity, accompanied
689 by nucleolar disruption, impairs synapsis and significantly reduced oocyte production (**Figure 2-3**).
690 Intriguingly, depletion of fibrillarin, a structural nucleolar protein, similarly inhibited meiotic synapsis and
691 reduced oogenesis, suggesting the critical importance of nucleolar activity during meiosis **(Figure 3, S4**).
692 Collectively, these findings strongly suggest that a nucleolar stress response mechanism directly impairs
693 meiotic progression, independently of downstream protein synthesis deficits.

694 **Chromatin remodeling drives meiotic defects in response to nucleolar disruption**

695 Oogenesis requires elaborate chromatin remodeling, including gradual chromosome condensation during
696 meiosis, and the spatial and temporal regulation of H3K4me3. Although many oogenic genes remain
697 transcriptionally quiescent in late-stage oocytes, epigenetic priming at the chromatin level is essential for
698 these genes to rapidly activate during zygotic genome activation. Thus, our study reveals a key non-
699 ribosomal function of the RNA Pol I activity, and nucleolar integrity, in coordinating these critical
700 epigenetic transitions.

701 Although nucleolar disruption clearly impacts chromatin organization, we did not observe a correlation
702 between promoter accessibility and mature mRNA levels (**Figure S5**). This is consistent with another study
703 in *C. elegans* that found no correlation between ATAC-seq signal and active transcription in isolated germ
704 cells [4], suggesting that chromatin accessibility alone does not fully account for gene expression regulation
705 in the germ line. Germline mRNA expression may instead be regulated by other mechanisms, including
706 22G-RNA and piRNA silencing (21U-RNAs) [72–74], inhibition of RNA Polymerase II carboxyl-terminal
707 domain phosphorylation by PIE-1 [75], and post-transcriptional 3'UTR regulation controlled by RNA-binding
708 proteins, such as PUF family proteins or GLD-1 [76–79]. Indeed, prophase-arrested oocytes remain
709 transcriptionally silent which coincides with PIE-1 re-localizing from the nucleolus to the nucleoplasm after

710 nucleolar dissolution [25]. Thus, premature nucleolar disruption may cause the untimely release of PIE-1,
711 reinforcing transcriptional silencing despite increased chromatin accessibility. This mechanism likely
712 explains why regions of differentially open chromatin do not become transcriptionally active upon RNA
713 Pol I depletion.

714 Despite the lack of immediate transcriptional consequences, our data suggest that disruptions in chromatin
715 conformation alone, driven by nucleolar cap formation, are sufficient to impair meiotic progression and
716 reduce oocyte production. Given the extensive chromatin reorganization required in meiotic cells compared
717 to other non-differentiating cell states, it is plausible that germ cells may be particularly vulnerable to such
718 significant disturbances in nuclear architecture, even if these do not immediately affect transcriptional
719 output.

720 **How nucleolar structure might drive meiotic chromatin dynamics**

721 Two potential mechanisms may explain why nucleolar disruption impair meiotic progression, particularly
722 through aberrant chromatin remodeling.

723 First, the disassembly of nucleolus via near complete depletion of RNA Pol I could release ribosomal
724 proteins or other factors (e.g. MDM2) that, in other organisms, stabilize P53 or similar pathways to trigger
725 cell cycle arrest [80,81]. Although *C. elegans* lacks a direct MDM2 homolog, analogous pathways may be at
726 play to prevent meiotic entry, potentially explaining the observed oogenesis defect. Indeed, our data show
727 no significant stabilization of the C. elegans p53 ortholog, CEP-1, upon nucleolar disruption, indicating
728 that any cell cycle arrest likely occurs independently of CEP-1/p53, possibly involving other checkpoint
729 mechanisms or signaling pathways.

730 Second, nucleolar caps may function as stress sensors for DNA damage or incompletely replicated rDNA,
731 activating surveillance pathways that stall meiotic progression. This model is supported by findings in other
732 systems showing that nucleolar stress can prompt G2 arrest through ATR-Chk-1 signaling, independent of
733 ribosome depletion [82]. In *C. elegans*, rDNA loci may become exposed prematurely when nucleolar structure
734 is compromised, leading to activation of ATM/ATR pathways and diverting double-strand break repair or
735 chromatin-modifying complexes toward rDNA repeats. Indeed, we observed increased ATM/ATR
736 checkpoint activation upon RNA Pol I depletion, supporting this interpretation. Given that proper ATM
737 and ATR activity is critical for organization of chromosomes along the cohesin axis and normal meiotic
738 progression [83,84], exposure of rDNA loci could disrupt the balance of ATM/ATR activity, leading to
739 prophase arrest in RPOA-2-depleted animals.

740 An additional possibility is that aberrant chromatin remodeling, particularly premature deposition of
741 H3K4me3 marks, could itself trigger ATM/ATR checkpoint signaling. Our results indicate that RNA Pol I
742 depletion causes significant chromatin remodeling at promoters of oogenesis specific genes as well as other
743 autosomal loci. This altered chromatin accessibility, driven by aberrant H3K4 methylation patterns, could
744 disrupt normal synaptonemal complex formation and homologous recombination processes [63]. Thus,
745 nucleolar stress induced redistribution of chromatin modifying enzymes, including H3K4
746 methyltransferases, may initiate a cascade in which aberrant chromatin structure leads to synaptic defects
747 and subsequent ATM/ATR-dependent checkpoint activation. However, since H3K4 methyltransferases can
748 localize to double-strand break sites [62], this stress-driven redistribution of repair machinery might also
749 underlie the misregulated H3K4me3 pattern observed in our study.

750 Ribosomal RNA transcription itself can also be regulated by epigenetic modifications at rDNA loci [85].
751 Small molecule inhibitors such as CX-5461 or low dose oxaliplatin alter rDNA chromatin and activate
752 DNA damage responses or senescence in a p53 independent manner [86,87]. Since these drugs concurrently
753 stabilize or damage G quadruplex structures and generate replication stress [88,89], their pleiotropic effects
754 complicate interpretation. In contrast, our inducible genetic depletion of RNA Pol I subunits allows us to
755 isolate the effects on genome-wide chromatin, revealing a clear link between Pol I loss, H3K4me3 mis-
756 patterning, ATM/ATR activation and defective oogenesis, which occur independently of ribosome
757 production.

758 **Spatiotemporal control of H3K4 methylation by the nucleolus during oogenesis**

759 Our work demonstrates that premature nucleolar disassembly during oogenesis impairs germ cell
760 maturation, primarily through its effects on chromatin remodeling. Specifically, the regulation of H3K4-
761 related chromatin dynamics is critical for oogenesis, as H3K4me3 levels need to gradually increase along
762 the distal-proximal axis to prime the promoters of genes required for zygotic genome activation [4].
763 Disruptions in the activity of H3K4 de/methylases have been linked to abnormal nuclear morphology,
764 reduced oocyte production, and inability to enter meiosis [11–13]. In agreement, we find that premature
765 nucleolar disruption weakens the H3K4 remodeling gradient, leading to defects in chromatin architecture
766 and oocyte production. This highlights a novel role for nucleolar integrity as a critical upstream regulator
767 of the spatiotemporal regulation of H3K4 methylation necessary for germ cell maturation.

768 Our gonadal ATAC-seq analyses further reveal that nucleolar disruption uniquely increases chromatin
769 accessibility at oogenesis genes, oogenesis-promoting EFL-1-binding sites, and promoters undergoing

770 H3K4me3 remodeling during oogenesis. We propose a model in which germ cells experiencing nucleolar
771 stress redirect H3K4 methyltransferases or other remodeling factors to the site of rDNA damage, thereby
772 depleting them from normal chromatin remodeling tasks. This shift may lead to hyper-accessible yet
773 transcriptionally inactive loci in the germ line, consistent with the disruption of the normal H3K4me3
774 gradient and oogenesis-related gene priming.

775 Furthermore, our single-cell analysis of H3K4me3 immunofluorescence reveals that the positive H3K4me3
776 gradient along the distal-proximal gonad axis is disrupted under nucleolar stress. This perturbation is
777 mediated by premature deposition of H3K4me3 in the distal region, further supporting the misregulation of
778 chromatin accessibility in oogenesis genes. However, without single-cell ATAC-seq resolution, it remains
779 unclear how chromatin accessibility changes are distributed along the gonad axis.

780 Although H3K4me3 represents a major dynamic mark in oocyte development, H3K27 methylation is also
781 critical for germ line maintenance, and these marks are generally mutually exclusive [4]. It remains possible
782 that misregulated heterochromatin marks, such as H3K27me3, contribute to the nucleolar-disruption
783 phenotype. Intriguingly, H3K27 methylation has been associated with the nucleolus in other contexts [67],
784 further hinting that a global shift in histone marks underlies the oogenesis defects we observed.

785 **Broad implications**

786 While our study focuses on *C. elegans,* nucleolar integrity and H3K4me3 remodeling during oogenesis are
787 evolutionary conserved in higher eukaryotes, including humans [5–10]. This suggests that nucleolus may play
788 a similarly critical, non-ribosomal role in female gametogenesis in other species. The sensitivity of meiotic
789 germ cells to nucleolar stress has significant implications for reproductive health [90], particularly in
790 individuals exposed to environmental stress, undergoing aging, or affected by ribosomopathies.

791 Our findings also highlight potential explanations for phenotypic differences observed in disorders linked
792 to Pol I components, such as Treacher Collins syndrome, which involves mutations in *POLR1B*, and
793 uniquely impacts neural crest proliferation and migration [91,92]. By uncovering how nucleolar driven
794 chromatin reorganization shapes germ cell maturation, we provide a conceptual framework for
795 understanding how disruptions in rDNA transcription can lead to specialized developmental deficits. More
796 broadly, understanding these nucleolar roles offers a window into the intersection of genome maintenance,
797 chromatin remodeling, and cell fate decisions across Metazoan development.

ACKNOWLEDGEMENTS

We thank Trevor F. Freeman for generating ATAC-seq libraries. We thank Ayush Desai and Ajay Panda for their assistance with imaging experiments and vector construction used in this study, respectively. We thank Sarinay Cenik lab members, Cenik lab members, Can Cenik, Arlen Johnson, Steve Vokes, and Keiko Torii for constructive criticism and discussions.

This work was supported by the UT CNS Catalyst Grant, National Institutes of Health (NIH) NIGMS (R35GM138340), and Welch Foundation (F-2133-20230405) grants to E.S.C. Some strains were provided by the CGC, which is funded by NIH Office of Research Infrastructure Programs (P40 OD010440).

AUTHOR CONTRIBUTIONS

R.M.T. and E.S.C. conceptualized the project and co-wrote the original manuscript. R.M.T., Q.Z., and E.S.C. revised the manuscript. Q.Z. and F.A. generated the RPOA-1 AID strain and dsRNAs. R.M.T. performed all imaging, immunostaining, data processing, and statistical analyses. Q.Z. performed crosses, injections, and all other molecular experiments. A.R. generated the ATAC-seq and RNA-seq libraries. E.S.C. supervised the project and acquired funding.

RESOURCE AVAILABILITY

Data availability

ATAC-seq and RNA-seq libraries are available through NCBI GEO, with accession codes GSE290498 and GSE290499, respectively.

Code availability

Original pipeline used for germ nuclei linearization and confocal intensity quantification is hosted on the GitHub repository: https://github.com/raqmejtru/germ-nuclei-linearization.

DECLARATION OF INTERESTS

The authors declare no competing interests.

821 **MAIN FIGURE TITLES AND LEGENDS**

822 **Figure 1. Auxin-inducible depletion of RNA Pol I subunits and ribosome assembly factors reveal that**
823 **nucleolar structure is dependent on pre-rRNA synthesis but not downstream ribosome maturation.**
824 **See also Figure S1.**

825 (**A-D**) Germline expression of fluorescently tagged RPOA-2 (**A**), RPOA-1 (**B**), GRWD-1 (**C**), and TSR-2
826 (**D**) proteins after control or auxin treatment. Dissected germ lines are outlined in white. Each strain's
827 control/auxin images were taken with identical exposure settings. Scale bar = 50 µm. (**E**) Distribution of
828 germ nuclei GFP intensity after auxin-inducible depletion of GFP-tagged RPOA-1/RPOA-2/GRWD-
829 1/TSR-2. Statistical comparisons performed using left-tailed Welch's two-sample *t*-tests. (**F**) Comparisons
830 of counts per million (CPM) reads across a simplified single copy of the ITS1 and ITS2 loci based on
831 gonadal RNA-seq (total RNA) after auxin-inducible depletion of RPOA-2/GRWD-1/TSR-2. Points
832 represent biological replicates (3 per condition, each consisting of 20 gonads); bars and error bars represent
833 the mean and SEM, respectively. (**G-H**) Germline nucleolar morphology (endogenous NUCL-1::mKate2)
834 after auxin-inducible depletion of RPOA-2 (**G**) or GRWD-1 (**H**). Germ lines are outlined in white; zoomed-
835 in nucleoli are shown in the right column. Scale bars = 50 µm (whole gonad) and 5 µm (zoomed nucleoli).

836 **Figure 2. Oocyte morphology and organization are impaired by reduced RNA Pol I activity,**
837 **independent from RNA Pol I's role in ribosome production. See also Figure S2.**

838 (**A**) Representative DIC images of adult germ lines after auxin-inducible depletion of RPOA-1/RPOA-
839 2/GRWD-1/TSR-2. Dotted lines highlight the proximal arm; triangles point to proximal oocytes. Scale bar
840 = 50 µm. (**B**) Graphical representation of proximal arm length and oocyte positions quantified in (**C-E**).
841 (**C-E**) Proximal arm lengths (**C**), proximal oocyte counts (**D**), and oocyte sizes (**E**) after auxin-inducible
842 depletion of RPOA-1/RPOA-2/GRWD-1/TSR-2. Each point represents a measurement from an individual
843 animal, normalized to the mean of each strain's control group. Crossbars represent SEM. All comparisons
844 were performed using two-tailed Welch's two-sample t-tests followed by Bonferroni corrections.

845 **Figure 3. Synaptonemal complex formation during the mitotic-to-meiotic germ cell transition is**
846 **dependent on Pol I activity, but not other ribosome processing steps. See also Figure S3 and S4.**

847 **(A)** Confocal images of transition zone nuclei expressing degron::GFP::RPOA-2, EmGFP::SYP-3, and
848 NUCL-1::mKate2 following control or auxin-inducible depletion of RPOA-2 (top two rows). Additionally,
849 we show non-treated nuclei from a wild-type genetic background (middle row) and zoomed-in nuclei from
850 RPOA-2-depleted and wild-type conditions (bottom row, labeled a-e). Scale bar = 5 µm (transition zone)

851 and 0.5 µm (zoomed-in nuclei). **(B)** Confocal images of transition zone nuclei expressing EmGFP::SYP-3
852 and NUCL-1::mKate2 48 hours post RNAi knockdown of a non-target locus (*wrmScarlet*), *nucl-1*, *grwd-*
853 *1*, *rpoa-2*, and *fib-1* (top), as well as zoomed-in nuclei from each condition (bottom). Scale bar = 5 µm
854 (transition zone) and 0.5 µm (zoomed-in nuclei). All images were taken with identical laser intensity; due
855 to decreased SYP-3 expression under knockdown of *grwd-1, rpoa-2,* and *fib-1*, we have increased the
856 brightness of these conditions to be more comparable to wild type.

857 **Figure 4. Disrupting RNA Pol I activity prematurely primes autosomal promoters in an accessible**
858 **state associated with oogenesis. See also Figure S5.**

859 (**A**) Venn diagram comparing the number of significantly more accessible (SMA) regions following
860 RPOA-2 depletion versus GRWD-1 depletion, based on an adjusted $p < 0.05$. (**B**) Genomic feature
861 annotations of ATAC-seq peaks. SMA regions after RPOA-2 or GRWD-1 depletion are predominantly
862 located within 1 kb of the nearest promoter. (**C**) Log_2 fold-change estimates of chromatin accessibility
863 based on gonadal ATAC-seq data from at least three biological replicates per condition, each composed
864 of 20 gonads. Each segment along the x-axis represents a genomic region. The number of differentially
865 accessible regions are noted in the plot legend based on an adjusted $p < 0.05$. Percentages represent the
866 proportion of differentially accessible peaks relative to the total number of called peaks per chromosome.
867 (**D**) Enrichment of gene ontology (GO) biological processes in genes exhibiting increased accessibility
868 after depletion of RPOA-2 or GRWD-1 (Hypergeometric test, FDR < 0.001). The term "gene" refers to
869 those associated with the nearest genomic feature annotation of each peak. (**E**) Overlap between peaks
870 that are SMA after RPOA-2 depletion and peaks near genes involved in oogenesis [53] (Hypergeometric
871 test). (**F**) Chromosomal distribution of genes involved in oogenesis [53] and SMA peaks after RPOA-2
872 depletion. (**G**) Alignment of the *C. elegans* EFL-1-binding site, human E2F-binding site, and the two
873 motifs enriched in SMA peaks after RPOA-2 depletion. (**H**) Genomic feature annotations of peaks
874 containing an EFL-1-binding site. (**I**) GO enrichment analysis for biological processes among genes with
875 promoter peaks that contain an EFL-1-binding site (Hypergeometric test, FDR < 0.05).

876 **Figure 5. Chromatin regions that become more accessible after reducing RNA Pol I activity display**
877 **patterns of H3K4me3 remodeling characteristic of the germ-to-oocyte transition. See also Figure S6.**

878 (**A**) Log_2 fold-change estimates of chromatin accessibility after RPOA-2 depletion in peaks annotated to
879 genes that undergo H3K4me3 remodeling during oogenesis, compared to a random subset of peaks. The
880 number of peaks in each set is specified by *n*, and means are denoted by an *x*. Statistical comparisons were

881 performed using right-tailed Welch's two-sample *t*-tests with Bonferroni corrections. (**B**) Metagene
882 analysis of mean $\log_2$ ATAC signal (RPOA-2 depletion/control) within 1 kb of genes that undergo
883 H3K4me3 remodeling during oogenesis. In gonads with reduced RNA Pol I activity, the shape of chromatin
884 accessibility signal within each cluster mirrors the shape of H3K4me3 remodeling associated with each
885 gene cluster. (**C**) Distribution of average H3K27me3, H3K36me3, and H3K4me3 ChIP signals from wild-
886 type germ cells or oocytes within ATAC-seq peaks that are significantly more accessible (SMA) after
887 RPOA-2 depletion, compared to signals within an identically-sized random subset of regions. Means are
888 denoted by an *x*. (**D**) Metagene plot displaying the average H3K27me3, H3K36me3, and H3K4me3 ChIP
889 coverage from wild-type germ cells or oocytes within 1 kb of genomic regions that are SMA after RPOA-
890 2 depletion, compared to coverage within an identically-sized random subset of promoter ATAC-seq peaks
891 that are not SMA. (**E**) Representative 3-D confocal projections of adult gonad arms with H3K4me3
892 immunostaining and DAPI after control treatment or RPOA-2 depletion. Dotted lines represent gonad
893 boundaries determined from T-PMT. Scale bar = 50 µm. (**F**) Using the example gonads from (**E**), we show
894 germ cell position along a linear gonad axis following implementation of a gonad linearization algorithm
895 (see Methods). Each point represents a germ cell detection; however, note that not all gonadal cells are
896 detected by the algorithm. The distal tip is represented by zero on the gonad axis, whereas the most proximal
897 tip of the gonad is variable based on biological size, gonad disruption during immunostaining, or gonad
898 placement on Z-plane. H3K4me3 intensity measurements are normalized to DAPI to account for
899 differences in permeability across gonads. (**G**) Linear relationship between germ cell position along the
900 gonadal axis (from distal to proximal end) and H3K4me3 signal intensity (relative to DAPI intensity or
901 scaled per-gonad), aggregated across all gonads. Spearman correlation coefficients are represented on the
902 plot. Linear models and overall correlations are based on data from 3,933 control cell detections and 8,134
903 depletion cell detections from 50 and 77 gonads, respectively. (**H**) Distribution of Spearman coefficients
904 estimating per-gonad positive correlations between cell position on the gonad axis and H3K4me3 intensity
905 (relative to DAPI intensity or scaled per-gonad). Mean and standard error are represented by red points and
906 crossbars. The number of gonads analyzed per condition are represented by *n*. A one-tailed Welch's two-
907 sample *t*-test suggests that on average, control gonads have a higher magnitude correlation than gonads
908 with reduced RNA Pol I activity (Benjamini-Hochberg adjusted *p*-values).

909 **Figure 6. Schematic model illustrating the non-ribosomal function of RNA Pol I during *C. elegans***
910 **oogenesis.**

911 Under normal conditions (left), RNA Pol I activity maintains nucleolar integrity, which supports the
912 establishment of a proper H3K4me3 gradient from the distal to proximal germ line. This gradient facilitates

913 meiotic synapsis and the progression of oogenesis, resulting in normal oocyte formation. When RNA Pol I
914 activity is reduced (right), nucleolar disruption leads to premature and ectopic H3K4me3 deposition,
915 aberrant oogenesis chromatin remodeling, and activation of ATM/ATR signaling independently of CEP-
916 1/p53-mediated apoptosis. This dysregulation interferes with meiotic cell-cycle perturbation and leads to
917 abnormal oogenesis, characterized by fewer and enlarged oocytes. The model proposes an epigenetic
918 feedback mechanism that links nucleolar function to germline genome integrity. Created in BioRender.
919 https://BioRender.com/oq1fz8k.

920 **METHODS**

921 **Strain generation**

922 Constructs and strains used in this study are listed in **Table S7-S8**, respectively.

923 The *mKate2* tagged *nucl-1* allele was constructed using Cas9 protein driven by *eft-3* promoter in pDD162
924 and gRNA targeting a genomic sequence in the C-terminus of *nucl-1* in pAR2, a derivative of pRB1017,
925 an empty vector for gRNA cloning. The sgRNA construct pAR2 was generated by the oligos ESC-AR-5
926 and ESC-AR-6. *nucl-1::mkate2::c1^sec^3xflag* (pAR1) was constructed for generating the knock-in into
927 the C-terminus of the *nucl-1* gene. The 5′ and 3′ homology arms were amplified ~500 bp upstream of *nucl-*
928 *1* stop codon using oligos ESC-AR-7 and ESC-AR-8, and ~500 bp downstream of stop codon using ESC-
929 AKP-40 and ESC-AKP-41. The repair templates were used to replace the ccdB in pDD285.

930 Oligos ESC-AKP-(7-8) were used to generate a sgRNA targeting the N-terminus of the *dao-5* gene (16 bp
931 from start codon) in pAKP2. The 5' homologous arm (500 bp upstream of *dao-5* start codon) and 3'
932 homologous arm (500 bp downstream of start codon) were amplified using oligos ESC-AKP-(1-4), and
933 subsequently used to replace the ccdB cassette in pDD282 to construct the repair template plasmid pAKP1.

934 The *degron*::*GFP*-tagged *rpoa-1* gene allele was constructed in a similar manner as above using pDD162
935 and gRNA targeting a genomic sequence in the C-terminus of *rpoa-1* in pQZ104. Oligos ESC-QZ-518 and
936 ESC-QZ-519 were used to anneal sgRNA. The following reagents were used to assemble the final repair
937 template pQZ103: 5′ homology arm (548 bp upstream of *rpoa-1* stop codon), 3′ homology arm (868 bp
938 downstream of *rpoa-1* stop codon) were amplified using oligos ESC-QZ-512, ESC-QZ-513, ESC-FA-20,
939 and ESC-FA-21. The 5′ homologue arm template was synthesized by a gBlock (IDT, ESC-QZ-511), while
940 the 3′ homology arm was amplified using genomic DNA.

941 All plasmids for microinjection were purified using the PureLink HiPure Plasmid Miniprep Kit (Invitrogen
942 #K210002). Oligo sequences used to generate these plasmids are in **Table S6**.

943 Strains generated through microinjection were prepared according to guidelines from [93]. To generate
944 ESC254, N2 animals were injected with a mix consisting of 50 ng/µL pDD162 (Cas9 vector), 50 ng/µL
945 gRNA pAKP2, 50 ng/µL *dao-5* repair template of pAKP1, and 5 ng/µL of pCFJ104 as an extrachromosomal
946 marker. The SEC was then excised by heat shock. To generate ESC770, N2 animals were injected with a
947 mix consisting of 50 ng/µL pDD162, 50 ng/µL gRNA pAR2, 50 ng/µL *nucl-1* repair template of pAR1,
948 and 5 ng/µL extrachromosomal marker L3785. Animals lacking the extrachromosomal array were heat-

949 shocked to remove the SEC. To generate ESC772, DLW109 animals were injected with a mix consisting
950 of 50 ng/µL pDD162, 50 ng/µL gRNA pRR13, 50 ng/µL *rpoa-2* repair template of pQZ43, and 5 ng/µL
951 extrachromosomal marker pCFJ104. To generate ESC829, DLW109 animals were injected with a mix
952 consisting of 50 ng/µL pDD162, 50 ng/µL gRNA pQZ104, 50 ng/µL *rpoa-1* repair template of pQZ103,
953 and 5 ng/µL extrachromosomal marker pCFJ104. Finally, animals without the extrachromosomal array
954 were heat-shocked to excise the SEC.

955 *WT/mIn1* males were crossed separately to ESC795, ESC772 and ESC796 strains to generate males
956 carrying *EmGFP::syp-3* transgene and *mKate2*-tagged *nucl-1*, as well as hermaphrodites carrying
957 *degron::GFP*-tagged *rpoa-2* or *degron::GFP*-tagged *grwd-1*. Both hermaphrodite genotypes were in the
958 *BFP*-tagged *TIR1* and *WT/mIn1* background. These males were then crossed to the corresponding
959 hermaphrodites to generate the ESC825 and ESC826 strains. We also crossed ESC772 to RB1025 to
960 generate ESC818, a strain carrying *set-2(ok952)* mutation in auxin-inducible *rpoa-2* background. *set-*
961 *2(ok952)* mutation was genotyped using the oligos ESC-QZ-515, 516, 517.

962 To visualize nucleolar structure while depleting RPOA-2 or GRWD-1, we crossed the *nucl-1::mKate2*
963 reporter (ESC770) into the RPOA-2 AID background (ESC772) and GRWD-1 AID background (ESC796)
964 to produce ESC794 and ESC797.

965 Lastly, to examine the co-localization of nucleolar structure and chromatin during meiosis, we crossed the
966 *nucl-1::mKate2* reporter (ESC770) into a background containing a reporter for the synaptonemal complex
967 (CA1218).

968 **Worm growth**

969 *C. elegans* strains were maintained on plates with agar and nematode growth media (NGM) that were
970 seeded with *Escherichia coli* strain OP-50. Animals were grown at 20°C for all experiments. Prior to
971 experiments, animals were synchronized either by bleach synchronization or by allowing adults to lay
972 embryos for two hours. The synchronized embryos were grown on NGM agar plates until they reached the
973 late L4 stage. At the late L4 stage, animals were transferred to control or auxin treatment plates for further
974 analysis.

975 **Auxin treatment**

976 To deplete our proteins of interest using the auxin-inducible degron system (AID) system, we used a natural
977 auxin (IAA) compound from Alfa Aesar (#A10556). A 400 mM stock solution was prepared in EtOH and

978 stored at −20°C. For auxin treatment plates, we diluted IAA to a 1 mM concentration in NGM agar, then
979 poured and let it solidify in plates. For control treatment plates, we diluted an equivalent volume of ethanol
980 into NGM agar, then also poured and let it solidify in plates. Once solidified, plates were seeded with OP-
981 50 and set to incubate at 20°C overnight to allow lawn growth. Synchronized late L4 worms were then
982 transferred onto control or auxin plates for 18 hours at 20°C. Prior to any subsequent experiments, a
983 qualitative assessment of GFP depletion was performed on a fluorescent dissection scope to ensure that
984 auxin treatment worked as expected. Efficient degradation of RPOA-2 and GRWD-1 proteins were
985 previously validated by western blotting within the experimental timeframe used in this study [43,65].

986 **Polysome fractionation**

987 L4 larvae grown on regular NGM plates were transferred to NGM plates with and without 1 mM IAA for
988 24 hours at 20°C. Animals were liquid nitrogen flash frozen in polysome lysis buffer (20 mM Tris-HCl pH
989 7.4, 150 mM NaCl, 5 mM MgCl2) and ground in liquid nitrogen (with mortar and pestle). The frozen worm
990 powder was thawed on ice and solubilized in polysome lysis buffer that was supplemented with 1 mM DTT,
991 100 µg/ml cycloheximide, 40 U/100 µl recombinant ribonuclease inhibitor (Invitrogen #10777019), 2
992 U/100 µl DNase (Invitrogen #AM2238). Lysates were loaded onto 10% to 45% sucrose gradients and spun
993 for 2.5 hours at 40,000 rpm using SW 41 Ti rotor in an ultracentrifugation system (Beckman Coulter). RNA
994 from monosome and polysome peaks was isolated using a density fractionation system (Brandel). The data
995 were used for the analysis in **Figure S1E.**

996 The following steps were performed to calculate reductions in polysome abundance in auxin-treated
997 samples relative to controls. We annotated thresholds on the fractionation curves generated above that
998 encompassed free RNA regions, along with the first three polysome curves. Based on these thresholds, we
999 calculated the area under the curve (AUC) for each region using the `AUC` function in R with parameter
1000 `method = 'trapezoid'` [94]. Normalized polysome abundance was calculated by dividing the polysome AUC
1001 by the free RNA AUC. We then compared this normalized abundance between auxin and control
1002 treatments.

1003 **RNAi by dsRNA injection**

1004 We performed RNAi by injecting dsRNA into L4-stage animals. To generate the dsRNA, we amplified the
1005 following genes (*rpoa-2*, *grwd-1*, *fib-1*, and *nucl-1*) from cDNA, and non-target control (*wrmScarlet*) from
1006 plasmid pGLOW39. *T7* promoters were added to both ends of the amplified fragments using appropriate
1007 primers (ESC-RR-174/175, ESC-QZ-524/525, ESC526/527, ESC-QZ-528/529, ESC-QZ-416/417) (**Table**

1008 **S7**). The dsRNA synthesis was performed using the MEGAscript T7 Transcription Kit (Invitrogen
1009 #AMB13345) following the manufacturer's instructions. We injected dsRNA (3µg/µl) into L4-stage
1010 animals of ESC772, COP262, TG12, and ESC795 strains. After injection, the animals were transferred to
1011 NGM plates and incubated at 20℃ for 48 hours prior to imaging. At least 20 worms were injected for each
1012 dsRNA condition.

1013 **Widefield and confocal imaging**

1014 Widefield and confocal images were captured using a STELLARIS 8 microscope (Leica Microsystems).
1015 When applicable, Z-stacks were transformed into average projections using LAS-X software (Leica
1016 Microsystems). For images that are presented for qualitative purposes, we adjusted the brightness and
1017 contrast to highlight features of interest, ensuring that adjustments are identical across
1018 treatments/conditions. Images used for statistical quantification were analyzed in their raw form without
1019 adjustments.

1020 **Quantification of GFP signal**

1021 Imaging slides were prepared by transferring worms onto an immobilizing solution (10 mM levamisole
1022 hydrochloride, Sigma-Aldrich #31742-250MG). Gonads were dissected by using a hypodermic needle to
1023 slice near the head region. GFP signal was captured using a 10X objective with a GFP filter with consistent
1024 intensity and exposure settings.

1025 CellProfiler v4.2.6 was used to segment individual nuclei and measure signal intensity based on the average
1026 signal of each segmented nucleus [95]. Statistical comparison of mean GFP intensity between control and
1027 auxin treatments was carried out using a one-tailed Welch two-sample *t*-test, performed with the `t.test`
1028 function in R [94,87].

1029 **Quantification of apoptotic corpses**

1030 Acridine orange (AO) staining was used to count apoptotic corpses in young adult germlines. First, L4s
1031 were transferred onto control or 1 mM IAA plates seeded with OP50 for 16 hours. We confirmed that the
1032 GFP signal was visibly reduced in the auxin-treated animals under a fluorescent dissection scope prior to
1033 continuing with AO staining. After 16 hours, each plate was spiked with 500 µL of AO stain prepared using
1034 2 µL of 10 mg/mL AO (Invitrogen™ #A1301) dissolved in 1 mL of M9 buffer. Animals were left to feed
1035 on the stain for one hour, and were subsequently transferred onto new control or 1 mM IAA plates to de-
1036 stain for an additional hour before live imaging in levamisole.

1037 Fluorescent microscopy was used to identify strong GFP signals characteristic of apoptotic corpses that
1038 retain a green AO signal. We counted the number of corpses per one gonad arm per animal, and used a
1039 Mann-Whitney *U*-test to compare the distribution of corpses across control and auxin-treated samples.

1040 **Quantification of germline morphology**

1041 After control or auxin treatment, animals were transferred to slides with an immobilizing agent (10 mM
1042 levamisole hydrochloride, Sigma-Aldrich #31742-250MG). We captured whole-worm images for body
1043 measurements using a 10X DIC objective and germline morphology images using a 63X DIC objective.
1044 Using ImageJ, we measured body area, the length of the proximal arm (from the edge of the "-1" oocyte to
1045 the edge of the U-shaped arm bend), and the length and area of the three most proximal oocytes based on
1046 eggshell boundaries [96]. Oocyte counts were measured by scanning vertical stacks for nuclear and eggshell
1047 boundaries while imaging. Statistical comparisons were performed with the `t.test` function in R [94].

1048 **Library preparation**

1049 After control or auxin treatment, worms were transferred onto a slide with an immobilizing solution (1 mM
1050 levamisole hydrochloride, Sigma-Aldrich #31742-250MG). Gonads were dissected by using a hypodermic
1051 needle to slice near the head region. Twenty dissected gonads were collected per replicate into ddH_2O.

1052 For RNA-seq, the dissected gonads were transferred to 1 mL of TRIzol (Thermo Fisher Scientific),
1053 vortexed, then incubated for 5 minutes at room temperature. RNA was extracted by adding 200 µL of
1054 chloroform to the lysate, spinning for 10 minutes at 15,000 rpm, and isolating the supernatant. The isolated
1055 RNA was precipitated overnight at −20°C using 50 mM sodium acetate, 5 mM $MgCl_2$, 15 mg/mL
1056 GlycoBlue™ Coprecipitant (Thermo Fisher Scientific #AM9515), and isopropanol. RNA pellets were
1057 washed in 80% ethanol and prepared using the SMARTer Stranded RNA-Seq kit (Takara #634839).
1058 Briefly, the libraries were prepared by fragmenting and converting RNA to cDNA, and PCR amplified.
1059 PCR amplification reactions were run as follows: 1 minute denaturation at 94°C, followed by 15-17 cycles
1060 with 15 seconds at 98°C, 15 seconds at 55°C, and 30 seconds at 68°C. After PCR amplification, the DNA
1061 libraries were further purified using Agencourt AMPure XP beads (Fisher Scientific #A63880). The
1062 resulting libraries were quantified using the Qubit™ dsDNA HS Assay Kit (Thermo Fisher Scientific
1063 #Q32851) and sequenced on a NovaSeq 6000 v1.5 SP flow cell (Illumina).

1064 For ATAC-seq, the dissected gonads were stained with DAPI (5 ng/µL in PBS), then loaded onto a
1065 hemocytometer for nuclei counting. A volume containing 50,000 nuclei was then mixed with 2.5 µL TDE1

1066 tagmentase. The tagmentation reaction was incubated at 37 °C for 30 minutes on a shaker. Immediately
1067 after, the reactions were cleaned using the Zymo DNA Clean & Concentrator-5 kit (Fisher #NC9674845).
1068 The cleaned and tagmented DNA was then amplified with Nextera i5 and i7 adapters using the NEBNext®
1069 High-Fidelity 2X PCR Master Mix (NEB M0541L). Amplification reactions were run as follows: 5 minute
1070 extension at 72°C; 30 second denaturing at 98°C; 18-19 cycles with 10 seconds at 98°C, 30 seconds at
1071 63°C, and 1 minute at 72°C; and a final extension of 10 minutes at 72°C. PCR products were cleaned to
1072 remove adapter contamination using the Zymo DNA Clean & Concentrator-5 kit. Library quality was
1073 assessed by checking nucleosome banding patterns on a gel, and passing libraries were subsequently
1074 cleaned using Agencourt AMPure XP beads. The resulting libraries were quantified using the Qubit™
1075 dsDNA HS Assay Kit and sequenced on a NovaSeq 6000 v1.5 SP flow cell (Illumina).

1076 **Quantification of rDNA transcription**

1077 Raw RNA-seq reads were trimmed with Trim Galore! v0.6.10 using default parameters [97]. HISAT2 v2.2.1
1078 was then used to build an index of the WBcel235 genome using the command `hisat2-build --seed 40` [98].
1079 To report all multimapping alignments to repetitive rDNA regions, reads were mapped using the command
1080 `hisat2 --seed 40 --all`. Alignments were coordinate sorted using Picard SortSam v3.1.1 with the command
1081 `-SORT_ORDER coordinate --CREATE_INDEX true` [99].

1082 To quantify rDNA transcription, we manually curated "gene" annotations for the two unique internal
1083 transcribed spacers (ITS) and appended them to the WBcel235 annotation. We assessed alignment counts
1084 to the modified annotation using featureCounts v2.0.6 with parameters `-t gene -g gene_id -M -O --fraction
1085 -p` [100]. A Welch two-sample *t*-test was performed to compare mean counts per million reads mapped to
1086 each ITS region as well as the entire 45S region using the `t.test` function in R [94].

1087 For a visual comparison of coverage in the rDNA region, we used bamCoverage v3.5.4 to normalize reads
1088 to average counts per million using the parameters `--normalizeUsing CPM --binSize 25` [101]. Coverage was
1089 later visualized in R using the Gviz v1.47.1 package [102].

1090 rDNA transcription was also quantified by RT-qPCR. L4-stage animals were treated with or without auxin
1091 for 24 hours. Total RNA was treated with TURBO DNase (Thermo Fisher Scientific #AM2238), followed
1092 by phenol/chloroform extraction to remove DNA contamination. Approximately 800 ng of purified RNA
1093 was used for first-strand cDNA synthesis using SuperScript III Reverse Transcriptase (Thermo Fisher
1094 Scientific #18080-093) with random primers. RT-qPCR was performed using specific primer pairs (**Table**

1095 **S6**) on the QuantStudio 7 Flex Real-Time PCR System (Thermo Fisher Scientific). Relative rDNA
1096 transcript levels were determined by normalization to mature 26S rRNA.

1097 **Identification of differentially expressed genes**

1098 Raw RNA-seq reads were trimmed with Trim Galore! v0.6.10 using default parameters [97]. HISAT2 v2.2.1
1099 was then used to build an index of the WBcel235 genome using the command `hisat2-build --seed 40` [98].
1100 Reads were mapped using the command `hisat2 --seed 40` with default parameters. Alignments were
1101 coordinate sorted using Picard SortSam v3.1.1 with the command `-SORT_ORDER coordinate --
1102 CREATE_INDEX true` [99]. Alignment counts were then summarized using featureCounts v2.0.6 with
1103 parameters `-t exon -g gene_id -p` [100]. Before further analyses, we filtered genes down to the 19,985 protein
1104 coding genes found in the WBcel235 annotation, and we also filtered out genes with low expression (less
1105 than 5 counts across 3 biological replicates). We evaluated differential gene expression using DESeq2
1106 v1.40.2 with an experimental design that accounted for strain and treatment [103]. Genes were considered
1107 differentially expressed if they had a Benjamini-Hochberg adjusted p-value < 0.05.

1108 **Identification of differentially accessible regions**

1109 Raw ATAC-Seq reads were trimmed, aligned, decontaminated, and quality assessed using the SRAtac
1110 v0.5.0 pipeline [65]. Before performing differential accessibility analyses, we used RUVSeq v1.34.0 to
1111 perform batch correction on mapped counts by computing estimated factors of unwanted variance against
1112 an empirical set of control genes [104]. We arbitrarily selected control genes with p-values greater than 0.75
1113 and an average count per million above 20 in at least 90% of samples, calculated with the `filterByExpr`
1114 function in edgeR v3.42.4 [105].

1115 To evaluate differentially accessible chromatin regions (DARs), we used DESeq2 v1.40.2 with an
1116 experimental design that accounted for strain, treatment, and the estimated factors of unwanted variation
1117 [103]. We compared DARs across non-depleted and depleted samples using a significance threshold of a
1118 Benjamini-Hochberg adjusted p-value < 0.05. To visualize DARs, we performed $\log_2$ fold-change
1119 shrinkage using DESeq2's `lfcShrink` function with apeglm v1.22.1 shrinkage estimators [106].

1120 **ATAC-seq genomic feature annotation**

1121 ATAC-seq peaks were annotated using the `annotatePeak` function in the ChIPseeker v1.36.0 package with
1122 modification `overlap = all` [107] in conjunction with the TxDb ce11 v3.4.6 reference database [108]. Results
1123 were visualized with the `plotAnnoBar` function in the clusterProfiler v4.12.0 package [109,110].

1124 **Differential analysis of functional gene ontology (GO) biological processes**

1125 For both ATAC-seq and RNA-seq, differential analysis of functional gene ontology (GO) biological
1126 processes were performed using the `compareCluster` function in the clusterProfiler v4.12.0 package using
1127 the following parameters: fun = 'enrichGO', ont = 'BP', pAdjustMethod = 'fdr', pvalueCutoff = 0.0001
1128 (ATAC) or 0.001 (RNA), qvalueCutoff = 0.0001 (ATAC) or 0.001 (RNA) [109,110]. Results were visualized
1129 using the `dotplot` function in the enrichplot v1.24.0 package using parameter showCategory = 3 [111].

1130 **Motif enrichment and characterization**

1131 The MEME-suite bed2fasta tool was used to add nucleic sequences to background and differentially
1132 accessible peaks based on the UCSC ce11 reference genome [112]. We used the MEME-suite STREME tool
1133 to enrich for ungapped motifs present in our peak sets with a *p*-value and *E*-value threshold of 0.05, an
1134 alignment around the center of the peak, and all other default parameters [113]. We used the MEME-suite
1135 Tomtom tool [114] to map the enriched motifs against the 842 TF motifs present in the TFBSshape database
1136 [54]. We classified significant motif-motif similarity based on Pearson correlation coefficients, an *E*-value
1137 threshold of 8.42, and all other default parameters. We further manually curated matches to combine
1138 redundant query motifs and their repeated hits, and to ensure that alignments were visibly cohesive.

1139 To identify genomic sites in our ATAC-seq data containing the *C. elegans* EFL-1 motif (MA0541.1), we
1140 used the MEME-suite FIMO v5.5.5 tool with parameters `--thresh 1.0E-4 --nrdb--` against our background
1141 set of peaks (i.e., all peaks across all samples called in SRAtac pipeline). We identified which peaks
1142 contained EFL-1 motifs by searching for overlaps between EFL-1 motif sites and peaks using the
1143 `findOverlaps` function with parameter `type = 'within'` in the GenomicRanges v1.56.1 package [115]. Genes
1144 with EFL-1 motifs in their promoter were analyzed for enrichment of GO biological processes using the
1145 enrichGO function in the in the clusterProfiler v4.12.0 package with parameters `pAdjustMethod = 'fdr',
1146 pvalueCutoff = 0.05, qvalueCutoff = 0.05` based on the annotation of the peak that the motif was located
1147 in [109,110]. Results were visualized using the `dotplot` function in the enrichplot v1.24.0 package using
1148 parameter showCategory = 3 [111].

1149 **Metagene analysis of histone ChIP-seq coverage**

1150 Isolated germ and oocyte histone ChIP-seq experiments used in this study are listed in **Table S9**.

1151 Raw ChIP-seq reads were downloaded from NCBI using the SRA Toolkit [116]. Reads were processed using
1152 the nf-core/chipseq pipeline with parameters: `--genome WBcel235 --broad_cutoff 0.01 --macs_fdr 0.001
1153 --nomodel` and `--extsize` between 147-250 [117,118]. If read length was known, we specified the `--
1154 read_length` parameter, otherwise we specified the effective genome size (`--macs_gsize 100286401`)
1155 estimated using the recommended `faCount` tool [119].

1156 Next, bigwigAverage v3.5.5 was used to compute an average bigwig coverage track for each antigen and
1157 cell type combination (i.e., oocyte H3K4me3 antigen, oocyte H3K4me3 input, etc.) using parameter `--
1158 scaleFactors` with the scale factors provided by the nf-core/chipseq pipeline [101]. Average $\log_2$ ratios of
1159 coverage across antigen/input samples were then computed using bigwigCompare v3.5.5 with parameter `-
1160 -operation log2` [101]. Additionally, an average $\log_2$ coverage score was computed across significantly more
1161 accessible peaks after RPOA-2 depletion and an identically-sized random subset of ATAC-seq peaks by
1162 intersecting bigwig scores using the `findOverlaps` function in the GenomicRanges v1.56.1 [115].

1163 Metagene profile plots were used to display the average $\log_2$ ratios of ChIP signal from isolated germ cells
1164 or oocytes across peaks that were significantly more accessible after RPOA-2 depletion, or across an
1165 identically-sized random subset of promoter ATAC-seq peaks that were not significantly more accessible.
1166 The tool computeMatrix v3.5.5 was used to generate coverage scores per peak using parameters `--
1167 referencePoint center --afterRegionStartLength 1000 --beforeRegionStartLength 1000 --binSize 25` [101].
1168 Metagene plots were displayed using plotProfile v3.5.5 with parameter `--perGroup` to summarize scores
1169 across germ versus oocyte cell types [101].

1170 **Analysis of chromatin accessibility across H3K4me3-remodeled gene clusters**

1171 Scaling (size) factors for ATAC-seq peak counts were computed using the relative log expression (RLE)
1172 normalization method from DESeq2 v1.40.2 [103]. Each sample's ATAC-seq coverage was re-scaled and
1173 binned into bigwigs for downstream visualization using bamCompare v3.5.5 with parameters `--scaleFactor
1174 (1/RLE size factor) --binSize 50` [101]. RLE-normalized coverage for depletion and control samples was
1175 aggregated using bigwigAverage v3.5.5, and subsequently $\log_2$ transformed using bigwigCompare v3.5.5
1176 `--operation log2` to interpret fold changes in coverage across depletion and control conditions [101].

1177 Metagene profile plots were used to display the average log_2 ratios of ATAC signal across the H3K4me3-
1178 remodeled gene clusters. The tool computeMatrix v3.5.5 was used to generate coverage scores per gene
1179 using parameters `scale-regions --afterRegionStartLength 1000 --beforeRegionStartLength 1000 --
1180 regionBodyLength 1000 --binSize 25` [101]. Metagene plots were displayed using plotProfile v3.5.5 with
1181 parameter `--perGroup` to summarize scores across cluster 1, 2, and 3 gene sets [101].

1182 **Gonadal immunostaining**

1183 Prior to immunostaining, we confirmed that degron::GFP::RPOA-2 signal was visibly reduced in auxin-
1184 treated animals.

1185 H3K4me3 immunostaining was performed on tube-fixed dissected gonads from adult worms after control
1186 or auxin treatment. Briefly, gonads were dissected in a solution with levamisole and 0.05% Tween 20 in
1187 PBS (PBS-T). Dissected bodies were transferred to DNA LoBind™ Tubes (Eppendorf™ #022431021) and
1188 fixed for five minutes using 4% PFA, then washed three times with PBS-T. Next, gonads were
1189 permeabilized for fifteen minutes using 0.5% Triton X-100 in PBS-T. Gonads were then post-fixed using
1190 95% ethanol for five minutes at -20°C, washed three times in PBS-T, and blocked for one hour using 5%
1191 BSA in PBS-T. For primary antibody incubation, half of the gonads from each treatment condition were
1192 incubated overnight at 4°C in 2% BSA in PBS-T as a negative primary antibody control, while the other
1193 half were incubated overnight at 4°C using the primary antibody (Rabbit Anti-Histone H3 (tri-methyl K4)
1194 antibody (Abcam #ab8580), 1:250; Rabbit Phospho-(Ser/Thr) ATM/ATR Substrate Antibody (Cell
1195 Signaling #2851), 1:250) in 2% BSA in PBS-T. Gonads were subsequently washed three times using PBS-
1196 T and incubated at room temperature for two hours in the secondary antibody (For H3K4me3: 10 µg/mL
1197 of Goat Anti-Rabbit IgG (H+L) Cross-Absorbed Alexa Fluor™ 633 (Invitrogen™ #A-21070); for Phospho-
1198 (Ser/Thr) ATM/ATR Substrate: Goat anti-Rabbit IgG (H+L) Cross-Adsorbed Secondary Antibody, Alexa
1199 Fluor™ 555 (Thermo Fisher Scientific #A-21428), 1:200) in 2% BSA in PBS-T. Finally, gonads were
1200 washed three times with PBS-T and mounted onto slides using VECTASHIELD® Antifade Mounting
1201 Medium with DAPI (1.5 µg/mL) (Vector Laboratories #H120010).

1202 Immunostained gonads were imaged from the distal to proximal zones using 40X tile-scanned confocal Z-
1203 stacks of identical resolutions (2048x2048). All Z-stacks were forced to encompass 3 µm to minimize
1204 overlaps between nuclei for downstream nuclei segmentation. Additionally, all confocal images were
1205 captured using identical laser intensity and gain settings for downstream intensity quantification. We
1206 excluded imaging gonads that were not adequately laying flat on the slide, preventing us from completely

1207 capturing the distal to proximal zones within a 3 µm vertical space. Lastly, Z-stacks were transformed into
1208 average projections for further analyses using LAS-X software (Leica Microsystems).

1209 **Gonad linearization and H3K4me3 signal quantification**

1210 A custom QuPath v0.5.1 script was created to identify H3K4me3 signal intensity per nuclei following
1211 RPOA-2 control or depletion treatment. Briefly, gonads were manually annotated based on morphology
1212 from the T-PMT confocal channel, and these annotations were overlaid onto the corresponding DAPI
1213 channel. Gonad annotations were segmented using the `StarDist2D` function on the DAPI channel with the
1214 `dsb2018_heavy_augment.pb` model and parameters `normalizePercentiles(1, 99)`, `threshold(0.80)`,
1215 `pixelSize(0.1)`, and `cellExpansion(0)` [120,121]. Segmented nuclei annotations were copied to the H3K4me3
1216 channel. Average H3K4me3 and DAPI signal intensities within segmented nuclei were measured using the
1217 `addIntensityMeasurements` function with parameter `downsample = 0.1`. We converted average signal
1218 intensity to integrated signal intensity using the formula `integrated intensity = mean intensity * area of
1219 detected nuclei` to prevent nuclei detection area from biasing intensity comparisons across differently sized
1220 nuclei. Additionally, to account for differences in permeability across gonads during immunostaining (due
1221 to varying physical damage while vortexing, etc.), we normalized integrated H3K4me3 intensity to
1222 integrated DAPI signal, and separately to the maximum H3K4me3 intensity recorded per gonad.

1223 To analyze variation in H3K4me3 intensity from the distal to proximal zones, we employed a variation of
1224 a gonad linearization algorithm to track the location of each nuclei along a linearized gonad representation
1225 [122]. Briefly, in QuPath, a polyline skeleton was drawn from the distal tip to the most proximal end of the
1226 gonad. We computed perpendicular projections of each nucleus onto the nearest gonad skeleton segment
1227 and used this value to calculate the position of each nucleus along the gonad skeleton. We limited our
1228 analyses to nuclei that were within a linearized gonad length of 2,000 px.

1229 Lastly, for each gonad, we evaluated the positive non-parametric correlation between nuclei position along
1230 the linear gonad axis and integrated H3K4me3/DAPI intensity or per-gonad scaled H3K4me3 intensity
1231 using the `cor.test` function in R with parameters `method='spearman', alternative='greater', exact='false''
1232 and corrected for false positives using the `p.adjust` function in R with parameter `method='BH'' [94].

1233 **SUPPLEMENTAL TABLE LEGENDS**

1234 Table S1. Differential accessibility results from DESeq2 analysis comparing RPOA-2 control vs depletion
1235 conditions, as well as GRWD-1 control vs depletion conditions.

1236 Table S2. Gene ontology (GO) biological processes enriched in gene sets with increased accessibility after
1237 reducing RNA Pol I activity or ribosome biogenesis. (GeneRatio: the proportion of annotated genes that
1238 are significantly more accessible and belong to a specific GO set, relative to the total number of significantly
1239 more accessible genes. BgRatio: the proportion of genes in a specific GO set, relative to the total number
1240 of annotated *C. elegans* genes).

1241 Table S3. Ungapped sequence motifs enriched in differentially accessible regions (DAR) after reducing
1242 RNA Pol I activity or ribosome biogenesis, compared to motifs in background peaks. (Sites: the number
1243 and percentage of ATAC-seq regions in a DAR set that match the motif). (S.M.A. = significantly more
1244 accessible peaks, S.L.A. = significantly less accessible peaks)

1245 Table S4. Differentially expression results from DESeq2 analysis comparing RPOA-2 control vs depletion
1246 conditions, as well as GRWD-1 control vs depletion conditions.

1247 Table S5. Gene ontology (GO) biological processes enriched in differentially expressed genes (DEG) after
1248 reducing RNA Pol I activity or ribosome biogenesis. (GeneRatio: the proportion of DEGs that belong to a
1249 specific GO set, relative to the total number of DEGs. BgRatio: the proportion of genes in a specific GO
1250 set, relative to the total number of annotated C. elegans genes).

1251 Table S6. Oligonucleotides used in this study.

1252 Table S7. Constructs used in this study.

1253 Table S8. Strains generated and used in this study.

1254 Table S9. Data sets used in this study.

1255 **REFERENCES**

1256 1. Hamatani T, Carter MG, Sharov AA, Ko MSH. Dynamics of Global Gene Expression Changes
1257 during Mouse Preimplantation Development. *Developmental Cell*. 2004;6(1):117-131.
1258 doi:10.1016/S1534-5807(03)00373-3

1259 2. Vastenhouw NL, Cao WX, Lipshitz HD. The maternal-to-zygotic transition revisited. *Development*.
1260 2019;146(11):dev161471. doi:10.1242/dev.161471

1261 3. Tadros W, Lipshitz HD. The maternal-to-zygotic transition: a play in two acts. *Development*.
1262 2009;136(18):3033-3042. doi:10.1242/dev.033183

1263 4. Mazzetto M, Gonzalez LE, Sanchez N, Reinke V. Characterization of the distribution and dynamics
1264 of chromatin states in the C. elegans germline reveals substantial H3K4me3 remodeling during
1265 oogenesis. *Genome Res*. Published online December 26, 2023. doi:10.1101/gr.278247.123

1266 5. Blythe SA, Cha SW, Tadjuidje E, Heasman J, Klein PS. β-catenin Primes Organizer Gene
1267 Expression By Recruiting a Histone H3 Arginine 8 Methyltransferase, Prmt2. *Dev Cell*.
1268 2010;19(2):220-231. doi:10.1016/j.devcel.2010.07.007

1269 6. Vastenhouw NL, Zhang Y, Woods IG, et al. Chromatin signature of embryonic pluripotency is
1270 established during genome activation. *Nature*. 2010;464(7290):922-926. doi:10.1038/nature08866

1271 7. Zhang Y, Vastenhouw NL, Feng J, et al. Canonical nucleosome organization at promoters forms
1272 during genome activation. *Genome Res*. 2014;24(2):260-266. doi:10.1101/gr.157750.113

1273 8. Dahl JA, Jung I, Aanes H, et al. Broad histone H3K4me3 domains in mouse oocytes modulate
1274 maternal-to-zygotic transition. *Nature*. 2016;537(7621):548-552. doi:10.1038/nature19360

1275 9. Zhang B, Zheng H, Huang B, et al. Allelic reprogramming of the histone modification H3K4me3 in
1276 early mammalian development. *Nature*. 2016;537(7621):553-557. doi:10.1038/nature19361

1277 10. Xia W, Xu J, Yu G, et al. Resetting histone modifications during human parental-to-zygotic
1278 transition. *Science*. 2019;365(6451):353-360. doi:10.1126/science.aaw5118

1279 11. Laranjeira AC, Berger S, Kohlbrenner T, Greter NR, Hajnal A. Nutritional vitamin B12 regulates
1280 RAS/MAPK-mediated cell fate decisions through one-carbon metabolism. *Nat Commun*.
1281 2024;15(1):8178. doi:10.1038/s41467-024-52556-3

1282 12. Xiao Y, Bedet C, Robert VJP, et al. Caenorhabditis elegans chromatin-associated proteins SET-2
1283 and ASH-2 are differentially required for histone H3 Lys 4 methylation in embryos and adult germ
1284 cells. *Proceedings of the National Academy of Sciences*. 2011;108(20):8305-8310.
1285 doi:10.1073/pnas.1019290108

1286 13. Käser-Pébernard S, Müller F, Wicky C. LET-418/Mi2 and SPR-5/LSD1 Cooperatively Prevent
1287 Somatic Reprogramming of C. elegans Germline Stem Cells. *Stem Cell Reports*. 2014;2(4):547-559.
1288 doi:10.1016/j.stemcr.2014.02.007

1289 14. Dubois ML, Boisvert FM. The Nucleolus: Structure and Function. In: Bazett-Jones DP, Dellaire G,
1290 eds. *The Functional Nucleus*. Springer International Publishing; 2016:29-49. doi:10.1007/978-3-
1291 319-38882-3_2

1292 15. Korčeková D, Gombitová A, Raška I, Cmarko D, Lanctôt C. Nucleologenesis in the Caenorhabditis
1293 elegans Embryo. *PLOS ONE*. 2012;7(7):e40290. doi:10.1371/journal.pone.0040290

1294 16. Bjerregaard B, Maddox-Hyttel P. Regulation of ribosomal RNA gene expression in porcine oocytes.
1295 *Animal Reproduction Science*. 2004;82-83:605-616. doi:10.1016/j.anireprosci.2004.04.023

1296 17. Fuchs J, Loidl J. Behaviour of nucleolus organizing regions (NORs) and nucleoli during mitotic and
1297 meiotic divisions in budding yeast. *Chromosome Res*. 2004;12(5):427-438.
1298 doi:10.1023/B:CHRO.0000034726.05374.db

1299 18. Fulka H, Rychtarova J, Loi P. The nucleolus-like and precursor bodies of mammalian oocytes and
1300 embryos and their possible role in post-fertilization centromere remodelling. *Biochemical Society*
1301 *Transactions*. 2020;48(2):581-593. doi:10.1042/BST20190847

1302 19. Kresoja-Rakic J, Santoro R. Nucleolus and rRNA Gene Chromatin in Early Embryo Development.
1303 *Trends in Genetics*. 2019;35(11):868-879. doi:10.1016/j.tig.2019.06.005

1304 20. Zatsepina OV, Bouniol-Baly C, Amirand C, Debey P. Functional and Molecular Reorganization of
1305 the Nucleolar Apparatus in Maturing Mouse Oocytes. *Developmental Biology*. 2000;223(2):354-
1306 370. doi:10.1006/dbio.2000.9762

1307 21. Xu D, Chen X, Kuang Y, et al. rRNA intermediates coordinate the formation of nucleolar vacuoles
1308 in C. elegans. *Cell Reports*. 2023;42(8). doi:10.1016/j.celrep.2023.112915

1309 22. Cenik ES, Meng X, Tang NH, et al. Maternal Ribosomes Are Sufficient for Tissue Diversification
1310 during Embryonic Development in C. elegans. *Developmental Cell*. 2019;48(6):811-826.e6.
1311 doi:10.1016/j.devcel.2019.01.019

1312 23. Sims J, Copenhaver GP, Schlögelhofer P. Meiotic DNA Repair in the Nucleolus Employs a
1313 Nonhomologous End-Joining Mechanism. *The Plant Cell*. 2019;31(9):2259-2275.
1314 doi:10.1105/tpc.19.00367

1315 24. Fulka H, Langerova A. The maternal nucleolus plays a key role in centromere satellite maintenance
1316 during the oocyte to embryo transition. *Development*. 2014;141(8):1694-1704.
1317 doi:10.1242/dev.105940

1318 25. Belew MD, Chien E, Michael WM. Characterization of factors that underlie transcriptional
1319 silencing in C. elegans oocytes. *PLOS Genetics*. 2023;19(7):e1010831.
1320 doi:10.1371/journal.pgen.1010831

1321 26. Turowski TW, Tollervey D. Cotranscriptional events in eukaryotic ribosome synthesis. *WIREs*
1322 *RNA*. 2015;6(1):129-139. doi:10.1002/wrna.1263

1323 27. Dash S, Lamb MC, Lange JJ, et al. rRNA transcription is integral to phase separation and
1324 maintenance of nucleolar structure. *PLOS Genetics*. 2023;19(8):e1010854.
1325 doi:10.1371/journal.pgen.1010854

1326 28. Lafontaine DLJ, Riback JA, Bascetin R, Brangwynne CP. The nucleolus as a multiphase liquid
1327 condensate. *Nat Rev Mol Cell Biol*. 2021;22(3):165-182. doi:10.1038/s41580-020-0272-6

1328 29. Mukherjee S, Firpo EJ, Wang Y, Roberts JM. Separation of telomerase functions by reverse
1329 genetics. *Proceedings of the National Academy of Sciences*. 2011;108(50):E1363-E1371.
1330 doi:10.1073/pnas.1112414108

1331 30. Son MY, Belan O, Spirek M, et al. RAD51 separation of function mutation disables replication fork
1332 maintenance but preserves DSB repair. *iScience*. 2024;27(4). doi:10.1016/j.isci.2024.109524

1333 31. Taddei A, Hediger F, Neumann FR, Bauer C, Gasser SM. Separation of silencing from perinuclear
1334 anchoring functions in yeast Ku80, Sir4 and Esc1 proteins. *The EMBO Journal*. 2004;23(6):1301-
1335 1312. doi:10.1038/sj.emboj.7600144

1336 32. Ginisty H, Amalric F, Bouvet P. Nucleolin functions in the first step of ribosomal RNA processing.
1337 *The EMBO Journal*. 1998;17(5):1476-1486. doi:10.1093/emboj/17.5.1476

1338 33. Roger B, Moisand A, Amalric F, Bouvet P. Nucleolin provides a link between RNA polymerase I
1339 transcription and pre-ribosome assembly. *Chromosoma*. 2003;111(6):399-407. doi:10.1007/s00412-
1340 002-0221-5

1341 34. Spaulding EL, Feidler AM, Cook LA, Updike DL. RG/RGG repeats in the C. elegans homologs of
1342 Nucleolin and GAR1 contribute to sub-nucleolar phase separation. *Nat Commun*. 2022;13(1):6585.
1343 doi:10.1038/s41467-022-34225-5

1344 35. Lee CC, Tsai YT, Kao CW, et al. Mutation of a Nopp140 gene dao-5 alters rDNA transcription and
1345 increases germ cell apoptosis in C. elegans. *Cell Death Dis*. 2014;5(4):e1158-e1158.
1346 doi:10.1038/cddis.2014.114

1347 36. Rog O, Dernburg AF. Direct Visualization Reveals Kinetics of Meiotic Chromosome Synapsis. *Cell*
1348 *Reports*. 2015;10(10):1639-1645. doi:10.1016/j.celrep.2015.02.032

1349 37. Smolikov S, Eizinger A, Schild-Prufert K, et al. SYP-3 Restricts Synaptonemal Complex Assembly
1350 to Bridge Paired Chromosome Axes During Meiosis in Caenorhabditis elegans. *Genetics*.
1351 2007;176(4):2015-2025. doi:10.1534/genetics.107.072413

1352 38. Eberhard R, Stergiou L, Hofmann ER, et al. Ribosome Synthesis and MAPK Activity Modulate
1353 Ionizing Radiation-Induced Germ Cell Apoptosis in Caenorhabditis elegans. *PLOS Genetics*.
1354 2013;9(11):e1003943. doi:10.1371/journal.pgen.1003943

1355 39. McCarter J, Bartlett B, Dang T, Schedl T. On the Control of Oocyte Meiotic Maturation and
1356 Ovulation in*Caenorhabditis elegans*. *Developmental Biology*. 1999;205(1):111-128.
1357 doi:10.1006/dbio.1998.9109

1358 40. Berry J, Weber SC, Vaidya N, Haataja M, Brangwynne CP. RNA transcription modulates phase
1359 transition-driven nuclear body assembly. *Proceedings of the National Academy of Sciences*.
1360 2015;112(38):E5237-E5245. doi:10.1073/pnas.1509317112

1361 41. Liao S, Chen X, Xu T, et al. Antisense ribosomal siRNAs inhibit RNA polymerase I-directed
1362 transcription in C. elegans. *Nucleic Acids Research*. 2021;49(16):9194-9210.
1363 doi:10.1093/nar/gkab662

1364 42. Korsholm LM, Gál Z, Nieto B, et al. Recent advances in the nucleolar responses to DNA double-
1365 strand breaks. *Nucleic Acids Research*. 2020;48(17):9449-9461. doi:10.1093/nar/gkaa713

1366 43. Zhao Q, Rangan R, Weng S, Özdemir C, Cenik ES. Inhibition of ribosome biogenesis in the
1367 epidermis is sufficient to trigger organism-wide growth quiescence independently of nutritional
1368 status in C. elegans. *PLOS Biology*. 2023;21(8):e3002276. doi:10.1371/journal.pbio.3002276

1369 44. Nousch M, Eckmann CR. Translational Control in the Caenorhabditis elegans Germ Line. In:
1370 Schedl T, ed. *Germ Cell Development in C. Elegans*. Springer; 2013:205-247. doi:10.1007/978-1-
1371 4614-4015-4_8

1372 45. Racher H, Hansen D. Translational control in the C. elegans hermaphrodite germ line. *Genome*.
1373 2010;53(2):83-102. doi:10.1139/G09-090

1374 46. Pushpa K, Kumar GA, Subramaniam K. Translational Control of Germ Cell Decisions. *Results*
1375 *Probl Cell Differ*. 2017;59:175-200. doi:10.1007/978-3-319-44820-6_6

1376 47. Iouk TL, Aitchison JD, Maguire S, Wozniak RW. Rrb1p, a Yeast Nuclear WD-Repeat Protein
1377 Involved in the Regulation of Ribosome Biosynthesis. *Molecular and Cellular Biology*.
1378 2001;21(4):1260-1271. doi:10.1128/MCB.21.4.1260-1271.2001

1379 48. Schütz S, Fischer U, Altvater M, et al. A RanGTP-independent mechanism allows ribosomal protein
1380 nuclear import for ribosome assembly. Hegde RS, ed. *eLife*. 2014;3:e03473.
1381 doi:10.7554/eLife.03473

1382 49. Awad D, Prattes M, Kofler L, et al. Inhibiting eukaryotic ribosome biogenesis. *BMC Biology*.
1383 2019;17(1):46. doi:10.1186/s12915-019-0664-2

1384 50. Bass HW, Marshall WF, Sedat JW, Agard DA, Cande WZ. Telomeres Cluster De Novo before the
1385 Initiation of Synapsis: A Three-dimensional Spatial Analysis of Telomere Positions before and
1386 during Meiotic Prophase. *Journal of Cell Biology*. 1997;137(1):5-18. doi:10.1083/jcb.137.1.5

1387 51. Chriss A, Börner GV, Ryan SD. Agent-based modeling of nuclear chromosome ensembles
1388 identifies determinants of homolog pairing during meiosis. *PLOS Computational Biology*.
1389 2024;20(5):e1011416. doi:10.1371/journal.pcbi.1011416

1390 52. MacQueen AJ, Villeneuve AM. Nuclear reorganization and homologous chromosome pairing
1391 during meiotic prophase require *C. elegans chk-2*. *Genes Dev*. 2001;15(13):1674-1687.
1392 doi:10.1101/gad.902601

1393 53. Reinke V, Gil IS, Ward S, Kazmer K. Genome-wide germline-enriched and sex-biased expression
1394 profiles in Caenorhabditis elegans. *Development*. 2004;131(2):311-323. doi:10.1242/dev.00914

1395 54. Chiu TP, Xin B, Markarian N, Wang Y, Rohs R. TFBSshape: an expanded motif database for DNA
1396 shape features of transcription factor binding sites. *Nucleic Acids Res*. 2020;48(D1):D246-D255.
1397 doi:10.1093/nar/gkz970

1398 55. Chi W, Reinke V. Promotion of oogenesis and embryogenesis in the C. elegans gonad by EFL-
1399 1/DPL-1 (E2F) does not require LIN-35 (pRB). *Development*. 2006;133(16):3147-3157.
1400 doi:10.1242/dev.02490

1401 56. Angus-Hill ML, Schlichter A, Roberts D, Erdjument-Bromage H, Tempst P, Cairns BR. A
1402 Rsc3/Rsc30 Zinc Cluster Dimer Reveals Novel Roles for the Chromatin Remodeler RSC in Gene
1403 Expression and Cell Cycle Control. *Molecular Cell*. 2001;7(4):741-751. doi:10.1016/S1097-
1404 2765(01)00219-2

1405 57. Albert B, Knight B, Merwin J, et al. A Molecular Titration System Coordinates Ribosomal Protein
1406 Gene Transcription with Ribosomal RNA Synthesis. *Molecular Cell*. 2016;64(4):720-733.
1407 doi:10.1016/j.molcel.2016.10.003

1408 58. Han M, Wei G, McManus CE, Hillier LW, Reinke V. Isolated C. elegans germ nuclei exhibit
1409 distinct genomic profiles of histone modification and gene expression. *BMC Genomics*.
1410 2019;20:500. doi:10.1186/s12864-019-5893-9

1411 59. McManus CE, Mazzetto M, Wei G, Han M, Reinke V. The zinc-finger protein OEF-1 stabilizes
1412 histone modification patterns and promotes efficient splicing in the Caenorhabditis elegans
1413 germline. *G3 (Bethesda)*. 2021;11(12):jkab329. doi:10.1093/g3journal/jkab329

1414 60. Tabuchi TM, Rechtsteiner A, Jeffers TE, Egelhofer TA, Murphy CT, Strome S. Caenorhabditis
1415 elegans sperm carry a histone-based epigenetic memory of both spermatogenesis and oogenesis. *Nat*
1416 *Commun*. 2018;9(1):4310. doi:10.1038/s41467-018-06236-8

1417 61. Li T, Kelly WG. A Role for Set1/MLL-Related Components in Epigenetic Regulation of the
1418 Caenorhabditis elegans Germ Line. Schübeler D, ed. *PLoS Genet*. 2011;7(3):e1001349.
1419 doi:10.1371/journal.pgen.1001349

1420 62. Nottke AC, Beese-Sims SE, Pantalena LF, Reinke V, Shi Y, Colaiácovo MP. SPR-5 is a histone
1421 H3K4 demethylase with a role in meiotic double-strand break repair. *Proc Natl Acad Sci USA*.
1422 2011;108(31):12805-12810. doi:10.1073/pnas.1102298108

1423 63. Herbette M, Mercier MG, Michal F, et al. The *C. elegans* SET-2/SET1 histone H3 Lys4 (H3K4)
1424 methyltransferase preserves genome stability in the germline. *DNA Repair*. 2017;57:139-150.
1425 doi:10.1016/j.dnarep.2017.07.007

1426 64. Herbette M, Robert V, Bailly A, et al. A Role for Caenorhabditis elegans COMPASS in Germline
1427 Chromatin Organization. *Cells*. 2020;9(9):2049. doi:10.3390/cells9092049

1428 65. Freeman TF, Zhao Q, Surya A, Rothe R, Cenik ES. Ribosome biogenesis disruption mediated
1429 chromatin structure changes revealed by SRAtac, a customizable end to end analysis pipeline for
1430 ATAC-seq. *BMC Genomics*. 2023;24(1):512. doi:10.1186/s12864-023-09576-y

1431 66. Al-Refaie N, Padovani F, Hornung J, et al. Fasting shapes chromatin architecture through an
1432 mTOR/RNA Pol I axis. *Nat Cell Biol*. 2024;26(11):1903-1917. doi:10.1038/s41556-024-01512-w

1433 67. Bersaglieri C, Kresoja-Rakic J, Gupta S, et al. Genome-wide maps of nucleolus interactions reveal
1434 distinct layers of repressive chromatin domains. *Nat Commun*. 2022;13(1):1483.
1435 doi:10.1038/s41467-022-29146-2

1436 68. Hua L, Yan D, Wan C, Hu B. Nucleolus and Nucleolar Stress: From Cell Fate Decision to Disease
1437 Development. *Cells*. 2022;11(19):3017. doi:10.3390/cells11193017

1438 69. Paredes S, Maggert KA. Ribosomal DNA contributes to global chromatin regulation. *Proceedings*
1439 *of the National Academy of Sciences*. 2009;106(42):17829-17834. doi:10.1073/pnas.0906811106

1440 70. Wang C, Ma H, Baserga SJ, Pederson T, Huang S. Nucleolar structure connects with global nuclear
1441 organization. *MBoC*. 2023;34(12):ar114. doi:10.1091/mbc.E23-02-0062

1442 71. Potapova TA, Gerton JL. Ribosomal DNA and the nucleolus in the context of genome organization.
1443 *Chromosome Res*. 2019;27(1):109-127. doi:10.1007/s10577-018-9600-5

1444 72. Bagijn MP, Goldstein LD, Sapetschnig A, et al. Function, Targets, and Evolution of Caenorhabditis
1445 elegans piRNAs. *Science*. 2012;337(6094):574-578. doi:10.1126/science.1220952

1446 73. Gu W, Shirayama M, Conte D, et al. Distinct Argonaute-Mediated 22G-RNA Pathways Direct
1447 Genome Surveillance in the *C. elegans* Germline. *Molecular Cell*. 2009;36(2):231-244.
1448 doi:10.1016/j.molcel.2009.09.020

1449 74. Shen EZ, Chen H, Ozturk AR, et al. Identification of piRNA Binding Sites Reveals the Argonaute
1450 Regulatory Landscape of the *C. elegans* Germline. *Cell*. 2018;172(5):937-951.e18.
1451 doi:10.1016/j.cell.2018.02.002

1452 75. Belew MD, Chien E, Wong M, Michael WM. The topoisomerase II/condensin II axis silences
1453 transcription during germline specification in *Caenorhabditis elegans*. Arbeitman M, ed. *G3:*
1454 *Genes, Genomes, Genetics*. Published online October 3, 2024:jkae236.
1455 doi:10.1093/g3journal/jkae236

1456 76. Crittenden SL, Bernstein DS, Bachorik JL, et al. A conserved RNA-binding protein controls
1457 germline stem cells in Caenorhabditis elegans. *Nature*. 2002;417(6889):660-663.
1458 doi:10.1038/nature754

1459 77. Diag A, Schilling M, Klironomos F, Ayoub S, Rajewsky N. Spatiotemporal m(i)RNA Architecture
1460 and 3′ UTR Regulation in the *C. elegans* Germline. *Developmental Cell*. 2018;47(6):785-800.e8.
1461 doi:10.1016/j.devcel.2018.10.005

1462 78. Merritt C, Rasoloson D, Ko D, Seydoux G. 3′ UTRs Are the Primary Regulators of Gene
1463 Expression in the C. elegans Germline. *Current Biology*. 2008;18(19):1476-1482.
1464 doi:10.1016/j.cub.2008.08.013

1465 79. Wickens M, Bernstein DS, Kimble J, Parker R. A PUF family portrait: 3′UTR regulation as a way
1466 of life. *Trends in Genetics*. 2002;18(3):150-157. doi:10.1016/S0168-9525(01)02616-6

1467 80. Deisenroth C, Franklin DA, Zhang Y. The Evolution of the Ribosomal Protein–MDM2–p53
1468 Pathway. *Cold Spring Harb Perspect Med*. 2016;6(12):a026138. doi:10.1101/cshperspect.a026138

1469 81. Hannan KM, Soo P, Wong MS, et al. Nuclear stabilization of p53 requires a functional nucleolar
1470 surveillance pathway. *Cell Reports*. 2022;41(5):111571. doi:10.1016/j.celrep.2022.111571

1471 82. Ma H, Pederson T. The nucleolus stress response is coupled to an ATR-Chk1–mediated G2 arrest.
1472 *MBoC*. 2013;24(9):1334-1342. doi:10.1091/mbc.e12-12-0881

1473 83. Li W, Yanowitz JL. ATM and ATR Influence Meiotic Crossover Formation Through Antagonistic
1474 and Overlapping Functions in Caenorhabditis elegans. *Genetics*. 2019;212(2):431-443.
1475 doi:10.1534/genetics.119.302193

1476 84. Yu Z, Kim HJ, Dernburg AF. ATM signaling modulates cohesin behavior in meiotic prophase and
1477 proliferating cells. *Nat Struct Mol Biol*. 2023;30(4):436-450. doi:10.1038/s41594-023-00929-5

1478 85. Santoro R, Grummt I. Molecular Mechanisms Mediating Methylation-Dependent Silencing of
1479 Ribosomal Gene Transcription. *Molecular Cell*. 2001;8(3):719-725. doi:10.1016/S1097-
1480 2765(01)00317-3

1481 86. Drygin D, Lin A, Bliesath J, et al. Targeting RNA Polymerase I with an Oral Small Molecule CX-
1482 5461 Inhibits Ribosomal RNA Synthesis and Solid Tumor Growth. *Cancer Res*. 2011;71(4):1418-
1483 1430. doi:10.1158/0008-5472.CAN-10-1728

1484 87. Nechay M, Wang D, Kleiner RE. Inhibition of nucleolar transcription by oxaliplatin involves
1485 ATM/ATR kinase signaling. *Cell Chemical Biology*. 2023;30(8):906-919.e4.
1486 doi:10.1016/j.chembiol.2023.06.010

1487 88. Xu H, Di Antonio M, McKinney S, et al. CX-5461 is a DNA G-quadruplex stabilizer with selective
1488 lethality in BRCA1/2 deficient tumours. *Nat Commun*. 2017;8(1):14432.
1489 doi:10.1038/ncomms14432

1490 89. Osmanoğulları SC, Forough M, Persil Çetinkol Ö, Arslan Udum Y, Toppare L. Electrochemical
1491 detection of Oxaliplatin induced DNA damage in G-quadruplex structures. *Analytical Biochemistry*.
1492 2023;671:115149. doi:10.1016/j.ab.2023.115149

1493 90. Fulka H, Mrazek M, Fulka J. Nucleolar dysfunction may be associated with infertility in humans.
1494 *Fertility and Sterility*. 2004;82(2):486-487. doi:10.1016/j.fertnstert.2003.12.042

1495 91. Sanchez E, Laplace-Builhé B, Mau-Them FT, et al. POLR1B and neural crest cell anomalies in
1496 Treacher Collins syndrome type 4. *Genet Med*. 2020;22(3):547-556. doi:10.1038/s41436-019-0669-
1497 9

1498 92. Trainor PA. Craniofacial birth defects: The role of neural crest cells in the etiology and
1499 pathogenesis of Treacher Collins syndrome and the potential for prevention. *American Journal of*
1500 *Medical Genetics Part A*. 2010;152A(12):2984-2994. doi:10.1002/ajmg.a.33454

1501 93. Dickinson DJ, Pani AM, Heppert JK, Higgins CD, Goldstein B. Streamlined Genome Engineering
1502 with a Self-Excising Drug Selection Cassette. *Genetics*. 2015;200(4):1035-1049.
1503 doi:10.1534/genetics.115.178335

1504 94. R: A Language and Environment for Statistical Computing. Published online 2023. https://www.R-
1505 project.org/

1506 95. Stirling DR, Swain-Bowden MJ, Lucas AM, Carpenter AE, Cimini BA, Goodman A. CellProfiler 4:
1507 improvements in speed, utility and usability. *BMC Bioinformatics*. 2021;22(1):433.
1508 doi:10.1186/s12859-021-04344-9

1509 96. Schneider CA, Rasband WS, Eliceiri KW. NIH Image to ImageJ: 25 years of image analysis. *Nat*
1510 *Methods*. 2012;9(7):671-675. doi:10.1038/nmeth.2089

1511 97. Martin M. Cutadapt removes adapter sequences from high-throughput sequencing reads.
1512 *EMBnet.journal*. 2011;17(1):10-12. doi:10.14806/ej.17.1.200

1513 98. Kim D, Paggi JM, Park C, Bennett C, Salzberg SL. Graph-based genome alignment and genotyping
1514 with HISAT2 and HISAT-genotype. *Nat Biotechnol*. 2019;37(8):907-915. doi:10.1038/s41587-019-
1515 0201-4

1516 99. Picard toolkit. Published online 2019. Accessed December 12, 2023.
1517 https://broadinstitute.github.io/picard/

1518 100. Liao Y, Smyth GK, Shi W. featureCounts: an efficient general purpose program for assigning
1519 sequence reads to genomic features. *Bioinformatics*. 2014;30(7):923-930.
1520 doi:10.1093/bioinformatics/btt656

1521 101. Ramírez F, Ryan DP, Grüning B, et al. deepTools2: a next generation web server for deep-
1522 sequencing data analysis. *Nucleic Acids Research*. 2016;44(W1):W160-W165.
1523 doi:10.1093/nar/gkw257

1524 102. Hahne F, Durinck S, Ivanek R, et al. Gviz: Plotting data and annotation information along genomic
1525 coordinates. Published online 2023. doi:10.18129/B9.bioc.Gviz

1526 103. Love MI, Huber W, Anders S. Moderated estimation of fold change and dispersion for RNA-seq
1527 data with DESeq2. *Genome Biology*. 2014;15(12):550. doi:10.1186/s13059-014-0550-8

1528 104. Risso D, Ngai J, Speed TP, Dudoit S. Normalization of RNA-seq data using factor analysis of
1529 control genes or samples. *Nat Biotechnol*. 2014;32(9):896-902. doi:10.1038/nbt.2931

1530 105. Chen Y, Lun ATL, Smyth GK. From reads to genes to pathways: differential expression analysis of
1531 RNA-Seq experiments using Rsubread and the edgeR quasi-likelihood pipeline. Published online
1532 August 2, 2016. doi:10.12688/f1000research.8987.2

1533 106. Zhu A, Ibrahim JG, Love MI. Heavy-tailed prior distributions for sequence count data: removing
1534 the noise and preserving large differences. *Bioinformatics*. 2019;35(12):2084-2092.
1535 doi:10.1093/bioinformatics/bty895

1536 107. Wang Q, Li M, Wu T, et al. Exploring Epigenomic Datasets by ChIPseeker. *Current Protocols*.
1537 2022;2(10):e585. doi:10.1002/cpz1.585

1538 108. Annotation package for TxDb object(s). Published online 2019. Accessed December 12, 2023.
1539 http://bioconductor.org/packages/TxDb.Celegans.UCSC.ce11.refGene/

1540 109. Wu T, Hu E, Xu S, et al. clusterProfiler 4.0: A universal enrichment tool for interpreting omics data.
1541 *The Innovation*. 2021;2(3):100141. doi:10.1016/j.xinn.2021.100141

1542 110. Yu G, Wang LG, Han Y, He QY. clusterProfiler: an R Package for Comparing Biological Themes
1543 Among Gene Clusters. *OMICS: A Journal of Integrative Biology*. 2012;16(5):284-287.
1544 doi:10.1089/omi.2011.0118

1545 111. Yu G, Gao CH. enrichplot: Visualization of Functional Enrichment Result. Published online 2024.
1546 https://yulab-smu.top/biomedical-knowledge-mining-book/

1547 112. Bailey TL, Johnson J, Grant CE, Noble WS. The MEME Suite. *Nucleic Acids Research*.
1548 2015;43(W1):W39-W49. doi:10.1093/nar/gkv416

1549 113. Bailey TL. STREME: accurate and versatile sequence motif discovery. *Bioinformatics*.
1550 2021;37(18):2834-2840. doi:10.1093/bioinformatics/btab203

1551 114. Gupta S, Stamatoyannopoulos JA, Bailey TL, Noble WS. Quantifying similarity between motifs.
1552 *Genome Biology*. 2007;8(2):R24. doi:10.1186/gb-2007-8-2-r24

1553 115. Lawrence M, Huber W, Pagès H, et al. Software for Computing and Annotating Genomic Ranges.
1554 *PLOS Computational Biology*. 2013;9(8):e1003118. doi:10.1371/journal.pcbi.1003118

1555 116. SRA Toolkit Development Team. SRA Toolkit.
1556 https://trace.ncbi.nlm.nih.gov/Traces/sra/sra.cgi?view=software

1557 117. Ewels PA, Peltzer A, Fillinger S, et al. The nf-core framework for community-curated
1558 bioinformatics pipelines. *Nat Biotechnol*. 2020;38(3):276-278. doi:10.1038/s41587-020-0439-x

1559 118. nf-core/chipseq. https://doi.org/10.5281/zenodo.3240506

1560 119. Kent J, UCSC Genome Browser Group. faCount.
1561 https://hgdownload.soe.ucsc.edu/admin/exe/linux.x86_64/faCount

1562 120. Bankhead P, Loughrey MB, Fernández JA, et al. QuPath: Open source software for digital
1563 pathology image analysis. *Sci Rep*. 2017;7(1):16878. doi:10.1038/s41598-017-17204-5

1564 121. Schmidt U, Weigert M, Broaddus C, Myers G. Cell Detection with Star-Convex Polygons. In:
1565 Frangi AF, Schnabel JA, Davatzikos C, Alberola-López C, Fichtinger G, eds. *Medical Image*
1566 *Computing and Computer Assisted Intervention – MICCAI 2018*. Springer International Publishing;
1567 2018:265-273. doi:10.1007/978-3-030-00934-2_30

1568 122. Toraason E, Adler VL, Kurhanewicz NA, et al. Automated and customizable quantitative image
1569 analysis of whole Caenorhabditis elegans germlines. *Genetics*. 2021;217(3):iyab010.
1570 doi:10.1093/genetics/iyab010

1571